Journal of Water Process Engineering 83 (2026) 109580

Contents lists available at ScienceDirect

Journal of Water Process Engineering

journal homepage: www.elsevier.com/locate/jwpe

Photocatalytic H_2O_2 production and doxycycline degradation via a *Z*-scheme $MoSi_2N_4$-$Bi_2O_2CO_3$ nanocomposites under visible light: Characterization mechanism, and toxicity evaluations

Rahila Batul [a], Ali Alkhafaji [b], Dheyaa J. Jasim [c], Pradeep Kumar Singh [d,*], Y.M. Fahmy [e], Mirsobit Odilov [f], Ibrahm Mahariq [g,h,**], Mukhtorjon Karimov [i], Nuraddin Abdullayev [j], Reda A. Haggam [k,*]

[a] *Department of Pharmaceutical Chemistry, College of Pharmacy, University of Hail, Saudi Arabia*
[b] *Advanced Technical College, University of Warith Al-Anbiyaa, Karbala, Iraq*
[c] *College of Engineering, University of Al Maarif, Al Anbar, 31001, Iraq*
[d] *Department of Mechanical Engineering, Institute of Engineering & Technology, GLA University, Mathura, UP, 281406, India*
[e] *Department of Chemical Engineering, College of Engineering, King Khalid University, Abha, 61411, Saudi Arabia*
[f] *Kimyo International University in Tashkent, Shota Rustaveli str. 156, Tashkent, 100121, Uzbekistan*
[g] *University College, Korea University, Seoul, 02481, South Korea*
[h] *Department of Medical Research, China Medical University Hospital, China Medical University, Taichung, Taiwan*
[i] *Urgench State University, 14, Kh. Alimdjan str, Urgench, 220100, Uzbekistan*
[j] *National University of Uzbekistan, Tashkent, 100174, Uzbekistan*
[k] *Department of Chemistry, Faculty of Science, Islamic University of Madinah, Madinah, 42351, Saudi Arabia*

ARTICLE INFO

Editor: Marta Pazos

Keywords:
Z-scheme photocatalyst
Hydrogen peroxide production
Doxycycline degradation
Visible-light photocatalysis
Reactive oxygen species

ABSTRACT

The simultaneous removal of persistent antibiotics and the in-situ generation of H_2O_2 are promising routes for integrated energy–environmental remediation. Herein, noble-metal-free *Z*-scheme $MoSi_2N_4$–$Bi_2O_2CO_3$ (MSN–BOC) nanocomposites were fabricated via a hydrothermal synthesis followed by ultrasonic self-assembly. Response-surface optimization of $MoSi_2N_4$ loading, hydrothermal temperature, and ultrasonic power identified MSN0.4–BOC as the optimal photocatalyst, achieving a H_2O_2 production rate of 610 $\mu mol.g^{-1}.h^{-1}$ and > 97% doxycycline (DOX) removal with 57% TOC mineralization under visible light. Comprehensive characterization (XRD, FTIR, Raman, N2 sorption, SEM/TEM, XPS, UV–Vis DRS, PL/TRPL, photocurrent, and EIS) revealed intimate interfacial contact, enlarged surface area, broadened visible-light absorption, prolonged carrier lifetimes, and minimized charge-transfer resistance in the composite. Mott–Schottky and valence-band XPS analyses, together with radical scavenging and ESR measurements, confirmed a direct *Z*-scheme charge-transfer pathway in which photogenerated electrons in $MoSi_2N_4$ drive the two-electron oxygen reduction to H_2O_2, while holes in $Bi_2O_2CO_3$ oxidize DOX via •O2− and •OH as the main reactive species. LC–MS identified the main degradation intermediates and plausible pathways, and ecotoxicity assays demonstrated a substantial decrease in acute and developmental toxicity of the transformation products compared with parent DOX. Cycling tests and post-reaction XRD verified the structural stability and reusability of MSN0.4–BOC. This work establishes $MoSi_2N_4$–$Bi_2O_2CO_3$ *Z*-scheme heterojunctions as efficient and durable platforms for coupled H_2O_2 production and antibiotic wastewater detoxification under solar-light irradiation.

1. Introduction

The ever-increasing demand for clean water and sustainable energy has placed immense pressure on both environmental systems and technological innovation [1–3]. Over the past decade, the uncontrolled discharge of pharmaceutical wastes—especially antibiotics such as doxycycline have emerged as a new class of persistent organic pollutants in aquatic ecosystems [4–6]. These compounds are chemically stable,

* Corresponding authors.
** Correspondence to: I. Mahariq, University College, Korea University, Seoul, 02481, South Korea.
E-mail addresses: pradeep.kumar@gla.ac.in (P.K. Singh), lbmmahariq@gmail.com (I. Mahariq), relhaggan@iu.edu.sa (R.A. Haggam).

https://doi.org/10.1016/j.jwpe.2026.109580
Received 5 January 2026; Received in revised form 23 January 2026; Accepted 24 January 2026

bioactive, and poorly biodegradable, allowing them to accumulate and threaten aquatic life while accelerating the evolution of antibiotic-resistant bacteria [7–9]. Addressing such complex contamination requires environmentally benign and highly efficient treatment strategies [10–12]. At the same time, the green synthesis of hydrogen peroxide (H_2O_2) has attracted widespread attention as a sustainable alternative to conventional chemical oxidants [13]. H_2O_2 is a clean, powerful, and selective oxidizing agent that decomposes into harmless water and oxygen, making it ideal for use in environmental remediation, chemical synthesis, and energy-related processes [14,15]. However, the traditional anthraquinone process used for industrial H_2O_2 production is energy-intensive and environmentally unfriendly [16]. Therefore, the development of a photocatalytic route that enables simultaneous H_2O_2 production and degradation of pharmaceutical contaminants under visible-light offers a promising, eco-friendly, and cost-effective solution for integrated energy–environmental applications [17,18].

Among the various methods developed for H_2O_2 synthesis, such as electrochemical reduction of oxygen and traditional anthraquinone oxidation, photocatalytic production has recently gained significant attention for its environmental compatibility and direct utilization of solar energy [19]. In a typical photocatalytic process, semiconductor materials absorb photons with sufficient energy to excite electrons from the valence band (VB) to the conduction band (CB), generating photoinduced electrons and holes [20,21]. The photogenerated electrons reduce dissolved O_2 through a two-electron oxygen reduction reaction (ORR) to produce H_2O_2, while the holes can oxidize sacrificial donors or organic pollutants [22]. The overall efficiency of this process largely depends on the semiconductor's light absorption capability, charge carrier mobility, and the separation dynamics of electron–hole pairs. However, the practical application of single-component photocatalysts is often limited by rapid charge-carrier recombination and insufficient redox potentials [23,24]. To overcome these drawbacks, constructing heterojunction systems has proven an effective strategy to accelerate charge transfer and enhance redox activity [25,26]. In particular, *Z*-scheme photocatalytic systems have emerged as a superior design because they mimic the natural photosynthetic electron flow, preserving the substantial reduction and oxidation abilities of both semiconductors [27]. By enabling efficient vectorial charge migration and suppressing recombination losses, Z-scheme heterojunctions provide an ideal platform for highly selective, sustainable H_2O_2 production coupled with pollutant degradation under visible-light irradiation [28].

Among various visible-light-responsive semiconductors, bismuth-based materials have attracted increasing attention due to their unique layered crystal structures, suitable band gaps, and excellent chemical stability [29]. In particular, $Bi_2O_2CO_3$, a member of the bismuth oxycarbonate family, has emerged as a promising photocatalyst owing to its strong oxidative capability, nontoxicity, and environmental compatibility [30]. Its crystal lattice consists of alternating $[Bi_2O2]^{2+}$ slabs and CO_3^{2-} layers, which generate an intrinsic internal electric field that promotes the migration of photogenerated charge carriers [31]. Moreover, $Bi_2O_2CO_3$ exhibits appropriate band-edge positions for both oxidation and reduction reactions under visible-light irradiation [32]. Nevertheless, its overall photocatalytic activity remains hindered by rapid electron–hole pair recombination and a relatively narrow light absorption range [33]. To overcome these intrinsic limitations, coupling $Bi_2O_2CO_3$ with a narrow-bandgap and high-mobility semiconductor is an effective strategy. $MoSi_2N_4$, a newly discovered two-dimensional (2D) layered material, has attracted significant attention as a highly stable and tunable photocatalyst [34]. It exhibits excellent optical absorption in the visible range, high carrier mobility, and outstanding chemical robustness, owing to its covalently bonded Mo–N–Si framework. The atomic-level thickness of $MoSi_2N_4$ also favor fast surface charge transfer and abundant active sites for redox reactions [35]. Integrating $MoSi_2N_4$ with $Bi_2O_2CO_3$ can therefore construct a *Z*-scheme heterojunction, in which photoinduced electrons from $Bi_2O_2CO_3$ recombine with holes from $MoSi_2N_4$, effectively preserving the strong reduction potential of $MoSi_2N_4$ and the oxidation strength of $Bi_2O_2CO_3$ [36]. Such a configuration is expected to facilitate efficient charge separation, broaden the light absorption spectrum, and synergistically enhance both H_2O_2 production and pharmaceutical pollutant degradation under visible-light illumination [37].

Over the past few years, extensive efforts have been devoted to developing efficient photocatalysts capable of operating under visible-light irradiation for environmental and energy-related applications. Considerable research attention has been focused on designing heterojunction architectures and surface-engineered materials to enhance light harvesting, accelerate charge migration, and suppress the recombination of photoinduced carriers. For instance, Zhou et al. [38] constructed 3D flower-like $Bi_2S_3/Bi_2O_2CO_3$ photocatalytic materials self-assembled from 2D nanosheets, achieving remarkable RhB degradation due to strong interfacial charge transfer between Bi_2S_3 and $Bi_2O_2CO_3$. Similarly, Wang et al. [37] fabricated a $BiOCl/Bi_2O_2CO_3$ S-scheme heterojunction via $[Bi_2O2]^{2+}$ slab sharing, attaining an outstanding H_2O_2 productivity of 2562.95 μmol g^{-1} h^{-1} and enhanced carrier separation confirmed by EPR and DFT analysis. Meanwhile, Zhao et al. [36] employed first-principles calculations to investigate a 2D $MoSi_2N_4/AlN$ heterojunction, revealing S-scheme carrier transfer, intrinsic electric-field-induced charge migration, and a high solar-to-hydrogen conversion efficiency of 15.21%. Furthermore, Chang et al. [39] elucidated hot carrier relaxation dynamics in $MoSi_2N_4$ monolayers, demonstrating ultrafast lifetimes of ~166 fs (electrons) and ~ 146 fs (holes), highlighting its potential for efficient photocatalytic energy conversion. In addition, Mo et al. [40] theoretically proposed a type-II $As_2C_3/MoSi_2N_4$ heterostructure exhibiting exceptional carrier mobility (~8.9×10^4 cm^2 V^{-1} s^{-1}) and suitable band alignment for overall water splitting. Likewise, Wang et al. [41] reported an $Ag/Bi/Bi_2O_2CO_3$ composite capable of simultaneously degrading tetracycline and inactivating antibiotic-resistant bacteria, with singlet oxygen ($^1O2$) as the dominant reactive species. These studies underscore the critical role of interfacial engineering, dimensional hybridization, and charge-transfer modulation in enhancing visible-light-driven photocatalytic efficiency. Nevertheless, challenges such as limited charge separation and dual-function coupling persist. Hence, developing robust *Z*-scheme heterojunctions that integrate strong redox capability, wide light absorption, and synergistic H_2O_2 production–pollutant degradation remains a compelling direction for next-generation sustainable photocatalytic systems.

Herein, a novel Z-scheme $MoSi_2N_4$–$Bi_2O_2CO_3$ photocatalyst was successfully fabricated via a controlled hydrothermal self-assembly process, enabling efficient in situ H_2O_2 production and simultaneous degradation of antibiotic contaminants under visible light. The developed system integrates the broad light-harvesting ability and abundant reactive sites of a two-dimensional semiconductor with the strong oxidation capability and structural stability of a layered bismuth-based material, forming intimate heterointerfaces that accelerate interfacial charge migration and suppress recombination losses. To gain deep insight into the correlation between structure and performance, the as-prepared materials were comprehensively characterized using XRD, Raman, FTIR, SEM, TEM, XPS, UV–Vis DRS, PL, BET, EIS, and ESR analyses. These complementary techniques confirmed the formation of a direct *Z*-scheme charge-transfer channel, which preserves the high redox potentials of both components and promotes selective two-electron oxygen reduction for H_2O_2 formation while efficiently oxidizing organic molecules. Radical scavenging and ESR experiments were further employed to clarify the reaction mechanism and identify the dominant reactive species. This study not only demonstrates a novel dual-functional photocatalytic platform for integrated H_2O_2 production and pollutant degradation but also offers valuable guidance for the rational design of next-generation metal-free *Z*-scheme heterostructures for green chemical synthesis and water purification.

2. Experimental section

2.1. Materials and chemicals

All chemicals used in this work were of analytical grade and employed without any further purification. Ammonium molybdate tetrahydrate ($(NH_4)_6Mo_7O_2{\cdot}4H_2O$), silicon nitride ($Si_3N_4$), bismuth nitrate pentahydrate ($Bi(NO_3)_3{\cdot}5H_2O$), sodium carbonate (Na_2CO_3), nitric acid (HNO_3), ethanol, and Doxycycline hydrochloride (DOX, ≥98%) were obtained from Aladdin Chemical Co. Deionized water was used as the solvent throughout all experiments.

2.2. Synthesis of $MoSi_2N_4$ nanosheets

Ultrathin $MoSi_2N_4$ nanosheets were obtained through a two-step solid–gas reaction followed by exfoliation. Initially, a stoichiometric mixture of ammonium molybdate and silicon nitride was homogenized in an agate mortar. The powder blend was transferred to a quartz tube and annealed under ammonia flow at 800 °C for 4 h to complete the nitridation. After natural cooling, the grayish product was repeatedly rinsed with deionized water and ethanol to eliminate residual by-products, then dried at 60 °C overnight. The dried solid was ultrasonicated in ethanol for 1 h to yield well-dispersed few-layer $MoSi_2N_4$ nanosheets.

2.3. Preparation of $Bi_2O_2CO_3$ microplates

$Bi_2O_2CO_3$ microplates were synthesized using a facile hydrothermal method [42]. Typically, 2 mmol of $Bi(NO_3)_3{\cdot}5H_2O$ was dissolved in 30 mL of dilute HNO_3 (0.1 M) to form a transparent solution, into which 1 mmol of Na_2CO_3 was slowly introduced under vigorous stirring. The resulting suspension was transferred to a Teflon-lined autoclave and heated to 160 °C for 10 h. After the reaction, the autoclave naturally cooled to ambient temperature. The white precipitate was collected by centrifugation, washed thoroughly with ethanol and water, and finally dried at 60 °C overnight to obtain pure $Bi_2O_2CO_3$ microplates.

2.4. Construction of $MoSi_2N_4$–$Bi_2O_2CO_3$ heterojunction

The $MoSi_2N_4$–$Bi_2O_2CO_3$ heterostructures were synthesized via an ultrasonic-assisted self-assembly process followed by hydrothermal treatment (Fig. 1). In a typical procedure, predetermined amounts of $MoSi_2N_4$ nanosheets (0.25, 0.67, and 1.50 g, corresponding to 20, 40, and 60 wt% with respect to $Bi_2O_2CO_3$) were dispersed in 50 mL of ethanol and ultrasonicated for 30 min to form a uniform suspension. Subsequently, 1.0 g of $Bi_2O_2CO_3$ microplates was added to the mixture, which was further ultrasonicated for another 30 min and magnetically stirred for 4 h to promote intimate interfacial contact. The suspension was then transferred into a Teflon-lined stainless-steel autoclave and subjected to hydrothermal treatment at 120 °C for 12 h. After cooling to room temperature, the solvent was evaporated at 80 °C under stirring, and the obtained powders were dried at 60 °C overnight. The resulting composites were labeled as MSN0.2–BOC, MSN0.4–BOC, and MSN0.6–BOC, corresponding to 20, 40, and 60 wt% $MoSi_2N_4$ loading, respectively.

2.5. Characterization techniques

This section is explained in supplementary materials (Text S1).

2.6. Photocatalytic H_2O_2 production tests

Hydrogen peroxide (H_2O_2) production via photocatalysis was tested under visible light in a Pyrex reactor with water cooling to keep the temperature at 25 °C. In a typical experiment, 50 mg of the photocatalyst was dispersed in 100 mL of deionized water containing 10 vol% ethanol as a sacrificial electron donor. Prior to illumination, the suspension was magnetically stirred in the dark for 30 min to ensure adsorption–desorption equilibrium and then purged with O_2 gas for 20 min to achieve oxygen saturation. A 300 W xenon lamp (Perfectlight PLS-SXE300C, $\lambda > 420$ nm) equipped with a UV-cut filter served as the visible-light source, and the light intensity at the reaction surface was calibrated to 100 mW·cm^{-2} using a radiometer. During irradiation, the suspension was continuously stirred to maintain homogeneity and prevent sedimentation. At predetermined time intervals (every 10 or 20 min), 3 mL aliquots were withdrawn using a gas-tight syringe, centrifuged at 8000 rpm for 5 min to remove suspended particles, and analyzed immediately for H_2O_2 concentration. The concentration of H_2O_2 was quantified by the titanium sulfate spectrophotometric method. In brief, 1 mL of the supernatant was mixed with 1 mL of 0.1 M $Ti(SO_4)_2$ solution in an acidic medium, yielding a yellow pertitanic acid complex. The absorbance was measured at 405 nm using a UV–Vis spectrophotometer (Shimadzu UV-2600), and the H_2O_2 concentration was determined from a pre-established calibration curve. The apparent rate of H_2O_2 formation was expressed as μmol·L^{-1}·min^{-1}, and the activity of different samples (pure $Bi_2O_2CO_3$, pure $MoSi_2N_4$, and $MoSi_2N_4$–$Bi_2O_2CO_3$ composites with varying loadings) was systematically compared. All H_2O_2 experiments were performed in an open-to-air reactor under ambient conditions, ensuring continuous availability of dissolved O_2. The H_2O_2 production rate was determined in a separate experiment without DOX under otherwise identical photocatalytic conditions to avoid interference from organics.

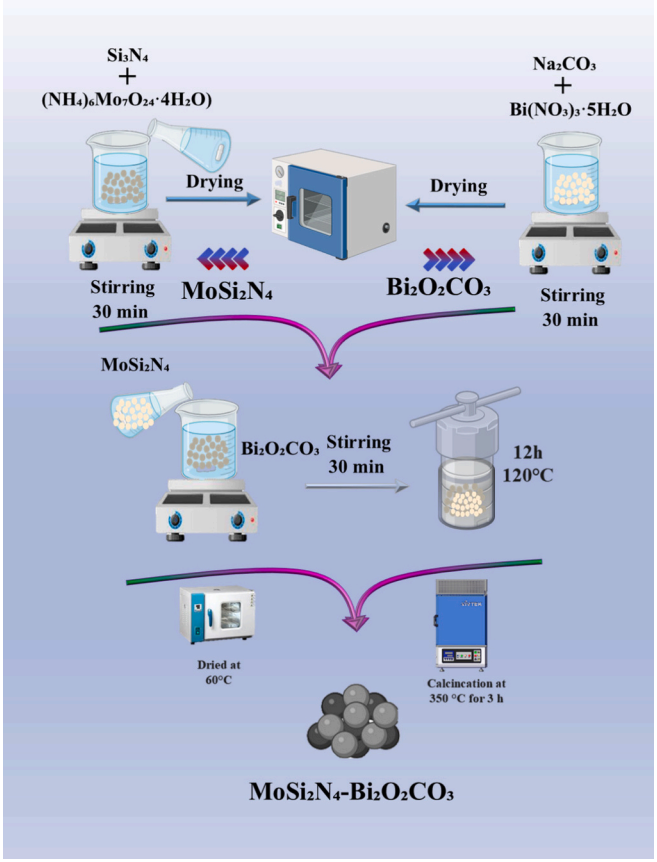

Fig. 1. Schematic diagram illustrating the synthesis process of $MoSi_2N_4$–$Bi_2O_2CO_3$ heterojunction.

2.7. Photocatalytic degradation of doxycycline

The photocatalytic degradation experiments were carried out under the same visible-light setup as the H_2O_2 generation tests to ensure

consistent conditions. In a standard experiment, 50 mg of photocatalyst was added to 100 mL of a 20 mg·L^{-1} DOX solution and stirred in the dark for 30 min to achieve adsorption–desorption equilibrium between DOX and the catalyst surface. Subsequently, the xenon lamp ($\lambda > 420$ nm) was switched on to initiate photocatalytic degradation. During illumination, 3 mL aliquots were withdrawn at fixed time intervals (e.g., every 10 min), centrifuged to remove the photocatalyst, and the residual DOX concentration was determined using UV–Vis spectrophotometry (Shimadzu UV-2600) by monitoring the absorbance at 345 nm the characteristic peak of doxycycline.

2.8. Reusability and stability evaluation

After each photocatalytic cycle, the catalyst was separated by centrifugation, washed thoroughly with deionized water and ethanol to remove surface residues or adsorbed intermediates, and then dried at 60 °C overnight before reuse. The activity loss, if any, was quantified by comparing the degradation efficiency and H_2O_2 generation rate across five consecutive runs. To further verify the structural stability of the photocatalyst after repeated use, the recycled samples were characterized by XRD to examine potential changes in the composites' crystallinity.

3. Results and discussion

3.1. Optimization of effective parameters for the synthesis of photocatalyst

Response Surface Methodology based on a Central Composite Design (RSM-CCD) was employed to systematically optimize the synthesis parameters, including $MoSi_2N_4$ loading, hydrothermal temperature, and ultrasonic power. This approach enabled evaluation of individual and interactive effects of the variables and identification of optimal conditions for photocatalytic performance. In Fig. 2a and Fig. 2d, the influence of MSN ratio is analyzed. The response plot in Fig. 2a shows that as the MSN ratio increases, H_2O_2 production initially increases, peaking at 40 wt%, with the highest production observed at 610 μmol·g^{-1}·h^{-1}, before slightly decreasing to 540 μmol·g^{-1}·h^{-1} at 50 wt%. This suggests that at 40 wt% MSN, the catalyst is optimally activated, with increased active sites leading to enhanced H_2O_2 generation [43]. However, beyond this ratio, the catalyst may reach saturation, diminishing its effectiveness. A similar trend is observed in Fig. 2d, where DOX degradation efficiency increases with the MSN ratio, peaking at 40 wt% and reaching approximately 88%. This peak at 40 wt% can be attributed to the increased catalyst surface area, which facilitates better interaction with and breakdown of DOX molecules [44]. However, after exceeding

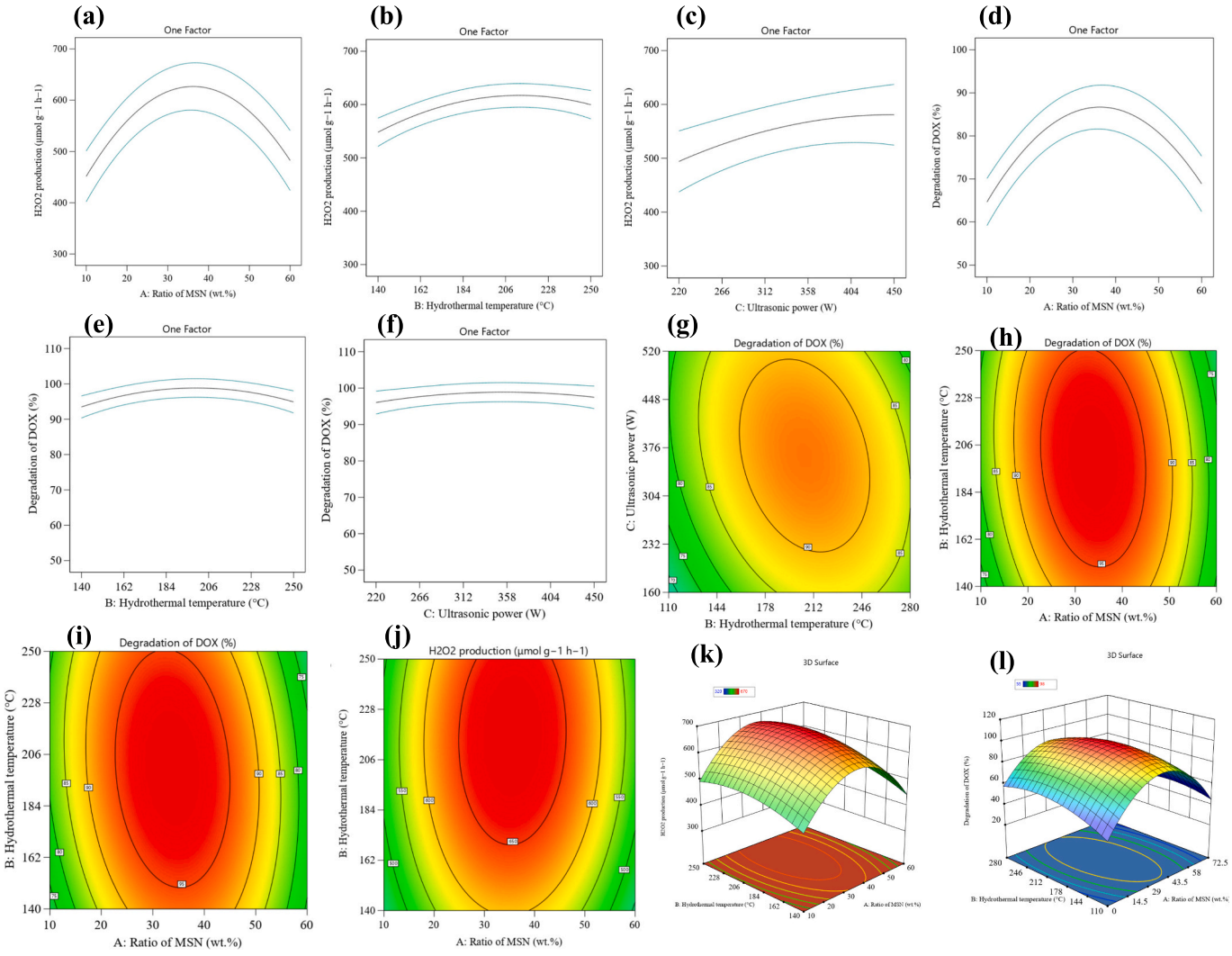

Fig. 2. (a–f) Response plots for individual factors demonstrating the impact of MSN ratio, hydrothermal temperature, and ultrasonic power on H_2O_2 generation and DOX degradation efficiency. (g–j) Contour plots showing the interactive effects of these parameters on DOX degradation. (k–l) 3D surface plots corresponding to the central composite design, illustrating the combined influence of the variables on the system's performance.

40 wt%, the efficiency decreases, suggesting that excess MSN may lead to reduced catalytic performance, possibly due to overloading or poor catalyst dispersion. These results highlight the importance of optimizing the MSN ratio, as a balance must be struck between providing sufficient active sites and avoiding excess that could reduce catalytic efficiency [45].

In Fig. 2b and Fig. 2e, the role of hydrothermal temperature on both H_2O_2 generation and DOX degradation is explored. Fig. 2b shows that as the hydrothermal temperature increases from 140 °C to 220 °C, H_2O_2 production rises from 550 $\mu mol \cdot g^{-1} \cdot h^{-1}$ to 610 $\mu mol \cdot g^{-1} \cdot h^{-1}$, before leveling off at 220 °C. This indicates that thermal activation plays a crucial role in enhancing catalytic activity, as higher temperatures likely facilitate the activation of reactive sites on the catalyst's surface, thereby improving the efficiency of H_2O_2 generation [46]. However, once the optimal temperature of 220 °C is reached, further temperature increases do not significantly boost H_2O_2 production, possibly because the catalyst's structural integrity is compromised or because a shift in the reaction mechanism reduces its effectiveness at higher temperatures [47]. Fig. 2e shows the effect of hydrothermal temperature on DOX degradation, where the degradation efficiency increases from 92% at 140 °C to 94% at 220 °C, before stabilizing. This further supports the idea that higher temperatures facilitate the activation of both the catalyst and the reaction environment, enhancing the breakdown of DOX molecules. The lack of further improvement beyond 220 °C suggests that the system reaches an optimal thermal condition where the catalytic process becomes saturated, and any additional heat does not result in greater degradation [48].

In Fig. 2c and Fig. 2f, the effects of ultrasonic power on H_2O_2 production and DOX degradation are examined. Fig. 2c illustrates that as ultrasonic power increases from 220 W to 450 W, H_2O_2 production rises significantly, peaking at 450 W with a production rate of 575 $\mu mol \cdot g^{-1} \cdot h^{-1}$. This trend can be attributed to enhanced cavitation at higher ultrasonic power, which improves mass transfer, promotes better catalyst dispersion, and increases the reaction rate, thereby enhancing H_2O_2 production [49]. However, beyond 450 W, the production rate shows no noticeable increase, suggesting that further increasing ultrasonic power might not significantly improve the efficiency of H_2O_2 generation. Similarly, Fig. 2f shows that DOX degradation increases with ultrasonic power, with the highest degradation efficiency of 95% observed at 450 W. Increasing ultrasonic power enhances degradation by generating more hydroxyl radicals, which break down DOX molecules. However, as with H_2O_2 production, further increases in ultrasonic power beyond 450 W yield diminishing returns, indicating an optimal ultrasonic power level for achieving the highest degradation efficiency without wasting energy [50].

The contour plots in Fig. 2g–j and Fig. S1a–c illustrate how pairs of operational parameters interactively influence DOX degradation and H_2O_2 production, revealing the optimal regions where catalyst performance is maximized. These contour maps clearly highlight the synergistic effects between MSN loading, hydrothermal temperature, and ultrasonic power. Furthermore, the 3D response surface plots in Fig. 2k–l and Fig. S1d–f provide a comprehensive visualization of the overall parameter interactions, enabling a clearer identification of global optimal conditions. Together, these graphical analyses demonstrate that efficient photocatalytic performance is achieved only through the simultaneous optimization of all three factors.

The analysis of variance (ANOVA) results summarized in Table S1 and Table S2 confirm that the quadratic response surface models developed for DOX degradation and H_2O_2 production are statistically significant ($F = 52.75$ and 43.11, $p < 0.0001$). In Table S1, the interaction term AB and the quadratic terms A^2, B^2, and C^2 significantly influence DOX removal efficiency, indicating strong curvature effects of the factors. Similarly, in Table S2, the hydrothermal temperature (B), ultrasonic power (C), and the quadratic terms (A^2, B^2, C^2) significantly affect H_2O_2 generation. The very low p-values (< 0.05) demonstrate that the models effectively describe the experimental data, although the significant lack-of-fit suggests minor deviations that could be improved by further model refinement [51].

3.2. Structural analysis

The X-ray diffraction (XRD) patterns presented in Fig. 3a provide essential insights into the crystallinity and phase composition of the samples. The XRD pattern of $Bi_2O_2CO_3$ in Fig. 3a exhibits several diffraction peaks located approximately at $2\theta = 13.1°$, 24.4°, 28.1°, 31.7°, 33.2°, 43.2°, 47.3°, 53.2°, and 57.6°, which correspond to the (002), (011), (013), (110), (112), (114), (020), (121), and (123) crystal planes, respectively [52]. These reflections match well with the standard orthorhombic phase of $Bi_2O_2CO_3$, confirming the successful formation of the crystalline bismuth oxycarbonate structure. The relatively sharp but moderate-intensity peaks indicate partial crystallinity with a layered structure. No impurity peaks are observed, suggesting high phase purity. In contrast, the XRD pattern of $MoSi_2N_4$ in Fig. 3a displays three distinct and sharp diffraction peaks located approximately at $2\theta = 33.2°$, 37.8°, and 52.9°, which correspond to the (100), (103), and (110) crystal planes, respectively [53]. These well-defined reflections are consistent with the reported hexagonal phase of $MoSi_2N_4$, confirming the formation of a highly crystalline layered structure. The high intensity and narrow width of the peaks indicate strong crystallinity and ordered atomic arrangement within the Mo–Si–N framework. The absence of additional peaks demonstrates phase purity, free of secondary oxides or nitrides. The diffraction profiles of MSN0.2–BOC, MSN0.4–BOC, MSN0.6–BOC, $MoSi_2N_4$, and $Bi_2O_2CO_3$ exhibit distinct diffraction peaks characteristic of their respective structural features. As the BOC content increases from MSN0.2–BOC to MSN0.6–BOC, the peak intensity and sharpness gradually increase, suggesting improved structural ordering and enhanced mesoporosity.

The Fourier transform infrared (FTIR) spectra in Fig. 3b reveal the characteristic functional groups and bonding environments of the prepared materials. The $MoSi_2N_4$ sample exhibits distinct absorption peaks at approximately 780 cm^{-1} and 900 cm^{-1}, corresponding to Si—N and Mo–Si–N vibrations, confirming the formation of covalent bonds between Si, Mo, and N atoms within the nitride lattice. The $Bi_2O_2CO_3$ spectrum shows prominent bands near 3400 cm^{-1} (O—H stretching), 1400–1450 cm^{-1} (asymmetric stretching of CO_3^{2-} groups), 820 cm^{-1} (out-of-plane bending of CO_3^{2-}), and 590 cm^{-1} (Bi—O stretching), verifying the coexistence of hydroxyl, carbonate, and bismuth–oxygen groups [54]. In the FTIR spectra of the MSN–BOC composites, all characteristic peaks of both $Bi_2O_2CO_3$ and $MoSi_2N_4$ can be clearly identified, indicating the successful combination of the two components without forming new impurity phases. A broad band around 3400 cm^{-1} is assigned to surface hydroxyl groups, which can facilitate interfacial interaction between $Bi_2O_2CO_3$ and $MoSi_2N_4$. The intensity of the CO_3^{2-} vibration near 1400 cm^{-1} gradually increases with higher $Bi_2O_2CO_3$ content (from MSN0.2–BOC to MSN0.6–BOC), suggesting enhanced incorporation of $Bi_2O_2CO_3$ within the composite structure.

The Raman spectra shown in Fig. 3c provide complementary information on the vibrational modes and bonding characteristics of the samples. In the $MoSi_2N_4$ spectrum, distinct peaks are observed at ~295 cm^{-1}, ~340 cm^{-1}, and ~ 520 cm^{-1}, assigned to Mo—N, Si–N–Mo, and Mo—Si vibrational modes, respectively, confirming the presence of the crystalline Mo–Si–N network [55]. The $Bi_2O_2CO_3$ sample exhibits characteristic modes at ~185 cm^{-1} (Bi—O lattice), ~380 cm^{-1} (Eg mode), and ~ 510 cm^{-1} (A_1g stretching), along with a weaker band near 1080 cm^{-1} attributed to the symmetric stretching of CO_3^{2-} groups [56]. For the MSN–BOC composites, the Raman spectra exhibit a combination of the characteristic vibrational modes of both $MoSi_2N_4$ and $Bi_2O_2CO_3$, demonstrating that the two components coexist without forming unwanted impurity phases. Notably, the intensity and position of certain peaks undergo slight variations compared with the pristine materials. The Mo—N and Si–N–Mo modes in the composite show minor peak broadening and slight red-shifts, which can be attributed to interfacial

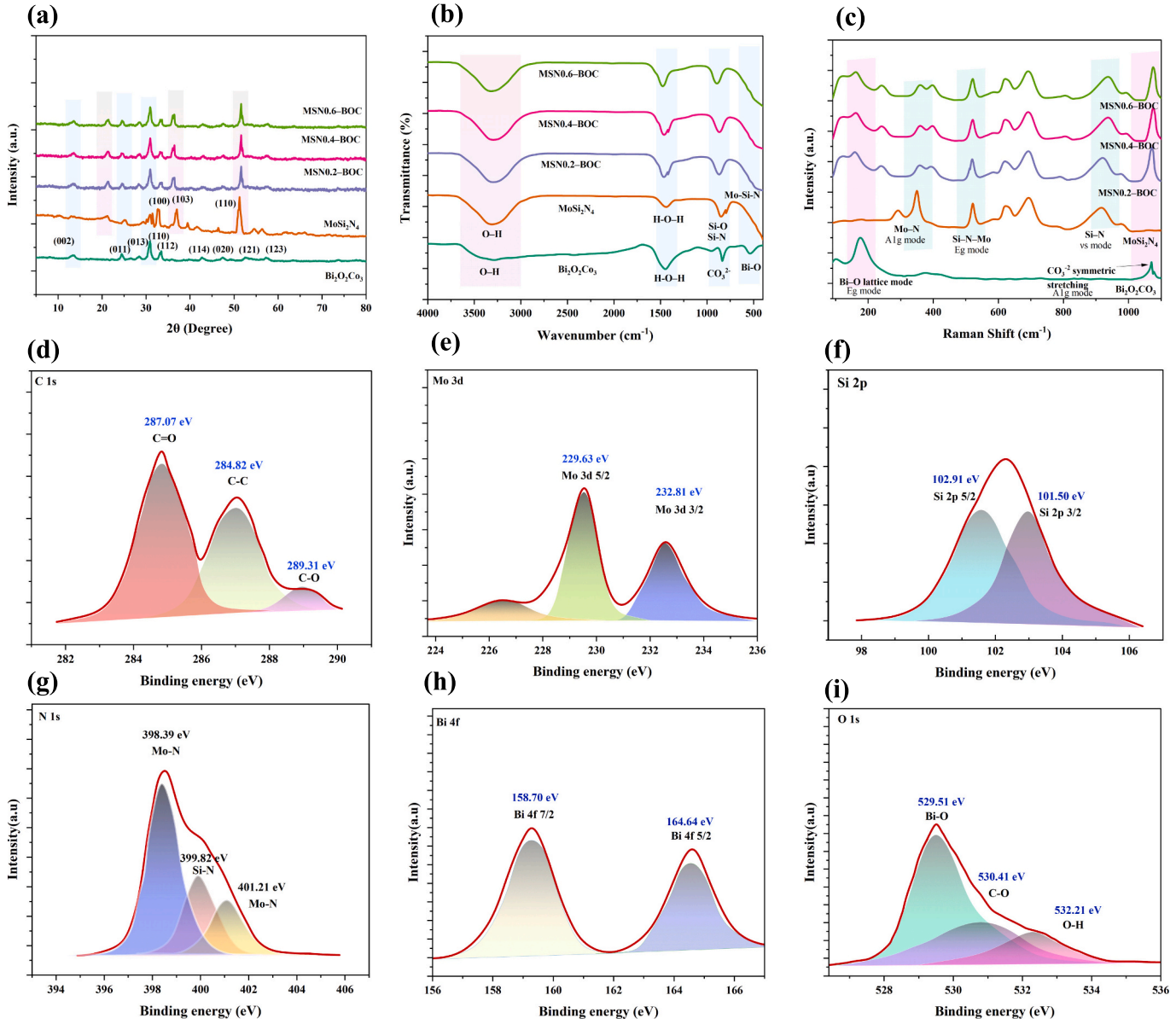

Fig. 3. (a) XRD patterns, (b) FTIR spectra, (c) Raman spectra. XPS spectra showing the binding energies of C 1 s (d), Mo 3d (e), Si 2p (f), N 1 s (g), Bi 4f (h), and O 1 s (i) for the MSN0.4–BOC samples.

strain, charge redistribution, and strong coupling between $MoSi_2N_4$ nanosheets and the $Bi_2O_2CO_3$ surface. Similarly, the Bi–O-related peaks of $Bi_2O_2CO_3$ become broader and slightly attenuated in the hybrid samples, suggesting partial modulation of the local coordination environment due to intimate heterojunction formation.

The N_2 adsorption–desorption isotherms in Fig. S2a exhibit type IV hysteresis loops, characteristic of mesoporous structures. Among all samples, $Bi_2O_2CO_3$ shows the highest nitrogen uptake, with a BET surface area of about 165 $m^2\ g^{-1}$, pore volume 0.31 $cm^3\ g^{-1}$, and average pore diameter 13.2 nm, indicating a highly porous framework. In contrast, $MoSi_2N_4$ exhibits the lowest surface area (≈42 $m^2\ g^{-1}$) and smallest pore volume (0.08 $cm^3\ g^{-1}$), reflecting its compact, less-porous crystalline structure. The MSN–BOC composites display intermediate characteristics: MSN0.2–BOC (130 $m^2\ g^{-1}$, 0.25 $cm^3\ g^{-1}$) and MSN0.4–BOC (95 $m^2\ g^{-1}$, 0.18 $cm^3\ g^{-1}$), confirming the presence of well-developed mesopores. The inset pore-size distributions reveal narrow peaks at 11–14 nm for the MSN–BOC and $Bi_2O_2CO_3$ samples, while $MoSi_2N_4$ exhibits a broader distribution near 9 nm. The trend $Bi_2O_2CO_3$ > MSN0.2–BOC > MSN0.4–BOC > $MoSi_2N_4$ demonstrates that increasing structural openness and surface hydroxylation enhance nitrogen adsorption. The high porosity of $Bi_2O_2CO_3$ provides abundant accessible channels for diffusion, whereas $MoSi_2N_4$'s dense structure limits gas uptake [57]. Overall, these results confirm that $Bi_2O_2CO_3$ possesses superior textural properties, while $MoSi_2N_4$ contributes mainly structural stability rather than surface area.

The XPS spectra in Fig. 3e-i provides detailed information on the chemical composition and bonding states of the materials. The Fig. S2b survey XPS spectrum reveals the presence of important elements, including Si, N, Mo, Bi, O, and C highlighting the complexity of the MSN0.4-BOC composite. The C 1 s XPS spectrum (Fig. 3d) shows three peaks at 284.82 eV (C—C), 287.07 eV (C=O), and 289.31 eV (C—O), confirming the presence of multiple carbon environments [58]. The Mo 3d spectrum in Fig. 3e for $MoSi_2N_4$ shows binding energies at 229.63 eV (Mo $3d_{5/2}$) and 232.81 eV (Mo $3d_{3/2}$), characteristic of molybdenum in the Mo—N environment, confirming the presence of $MoSi_2N_4$ [59]. The Si 2p spectrum in Fig. 3f at 101.50 eV (Si $2p_{3/2}$) and 102.91 eV (Si $2p_{5/2}$) indicates the presence of silicon in Si—N and Si—O bonding environments, which is consistent with the $MoSi_2N_4$ structure. The N 1 s

spectrum in Fig. 3g shows peaks at 398.39 eV (Mo—N) and 399.82 eV (Si—N), confirming nitrogen bonding to molybdenum and silicon in the nitride structure. The Bi 4f spectrum in Fig. 3h for $Bi_2O_2CO_3$ reveals peaks at 158.70 eV and 164.64 eV, confirming the presence of bismuth in the +3 oxidation state, bonded to oxygen [60]. The O 1 s spectrum in Fig. 3i for all materials shows peaks at 529.51 eV (Bi—O), 530.41 eV (C—O), and 532.21 eV (O—H), indicating the presence of oxygen in various bonding environments.

3.3. Morphological analysis

The structural and elemental characterization of $MoSi_2N_4$ and MSN0.4–BOC composite in Fig. 4 provides comprehensive insights into the materials' morphology, crystallinity, and elemental distribution, which are essential for understanding their potential applications. The SEM image of $MoSi_2N_4$ in Fig. 4a shows a crystalline, granular structure with tightly packed particles exhibiting smooth, well-defined surfaces. The particles appear uniformly sized, with grain boundaries clearly visible, indicating a highly ordered structure. The granular morphology of $MoSi_2N_4$ suggests that it is a high-purity, crystalline compound, which is beneficial for applications in catalysis, electronics, and high-temperature environments where stability and crystalline integrity are crucial. The particle size appears to range from 0.5 μm to 1.5 μm, with individual grains possibly smaller in the nanometer range, a characteristic of well-synthesized $MoSi_2N_4$ materials.

In contrast, the SEM image of MSN0.4–BOC (Fig. 4b) exhibits a distinct morphological structure compared with the pristine components. The MSN0.4–BOC composite displays an irregular and rough surface decorated with thin $MoSi_2N_4$ nanosheets intimately anchored on $Bi_2O_2CO_3$ particles. This architecture generates numerous interfacial voids and nanosized pores (approximately 5–10 nm) arising from the stacking of 2D layers and particle junctions. Such a porous and hetero-interfaced morphology facilitates charge separation and mass transfer, thereby enhancing photocatalytic performance. The observed agglomerates (2–5 μm) correspond to secondary assemblies of the hybrid nanosheets formed during the ultrasonic-assisted coupling process. Overall, the composite maintains a hierarchical structure that provides a high specific surface area and abundant active sites, making it well suited for photocatalytic and environmental remediation applications.

The TEM image of $MoSi_2N_4$ in Fig. 4c displays a highly crystalline, layered morphology composed of nanosheets with lateral sizes of approximately 50–100 nm. Clear lattice fringes can be observed, confirming the ordered atomic arrangement characteristic of the $MoSi_2N_4$ phase. The HR-TEM image of the MSN0.4–BOC composite (Fig. 4d) provides deeper insight into the nanostructure of the heterojunction. The image reveals intimate contact between $MoSi_2N_4$ nanosheets and $Bi_2O_2CO_3$ particles, forming coherent interfaces that facilitate charge transfer. Distinct lattice fringes with spacings of ~0.25 nm and ~ 0.31 nm are observed, corresponding to the (200) plane of $MoSi_2N_4$ and the (121) plane of $Bi_2O_2CO_3$, respectively, confirming the coexistence of both crystalline phases within the composite. The interfacial region appears uniform and well-defined, demonstrating that the incorporation of $MoSi_2N_4$ does not disrupt the crystalline structure of either component. Overall, the HR-TEM results verify the preservation of structural integrity after hybridization, and the formation of abundant hetero-interfaces is expected to promote efficient charge separation—an essential factor for enhanced photocatalytic activity. Moreover, the EDX elemental mapping results (Fig. 4e–j) further confirm the homogeneous spatial distribution of Mo, Si, N, Bi, O, and C across the MSN0.4–BOC composite.

3.4. Optical and electrochemical structure studies

The various characterization techniques shown in Fig. 5 provide crucial insights into the electronic structure, charge dynamics, and electrochemical properties of the materials MSN0.2-BOC, $Bi_2O_2CO_3$, MSN0.4-BOC, and $MoSi_2N_4$. Each figure reveals fundamental aspects of material performance that are vital for applications in catalysis, energy storage, and other surface-sensitive technologies. The UV–Vis absorption spectra in Fig. 5a show the light absorption capabilities of the

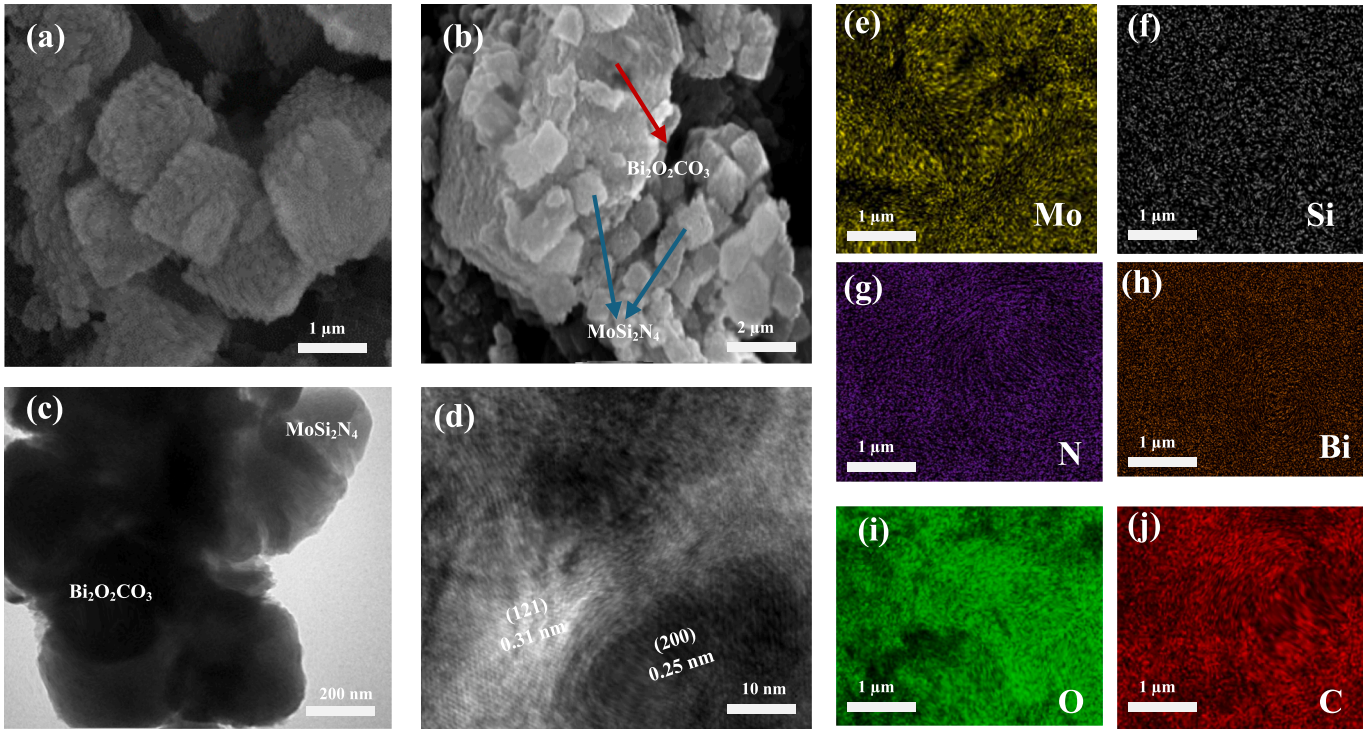

Fig. 4. (a) SEM image of $MoSi_2N_4$. (b) SEM image of the MSN0.4–BOC composite. (c) TEM image and (d) HR-TEM image of the MSN0.4–BOC composite. (e–j) EDS elemental mapping of the samples showing the distribution of key elements: (e) Mo, (f) Si, (g) N, (h) Bi, (i) O, and (j) C.

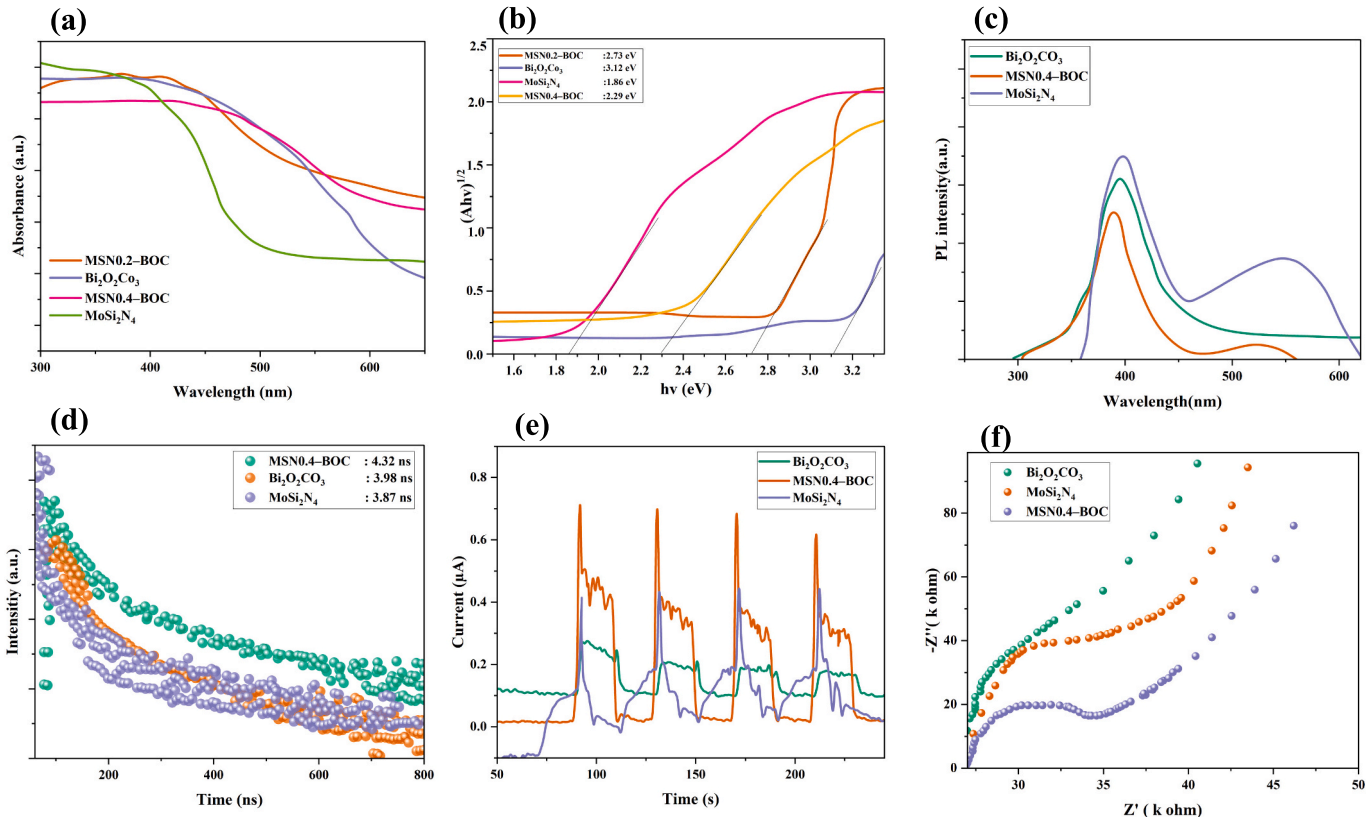

Fig. 5. (a) UV–Vis absorption spectra, (b) Tauc plots for band gap determination, (c) photoluminescence (PL) spectra, (d) time-resolved photoluminescence (TRPL) decay curves showing carrier recombination time, (e) photocurrent response under periodic light illumination, and (f) electrochemical impedance spectroscopy (EIS) Nyquist plots of MSN0.2-BOC, $Bi_2O_2CO_3$, MSN0.4-BOC, and $MoSi_2N_4$.

different materials across the UV–visible spectrum (300–600 nm). MSN0.2-BOC and MSN0.4-BOC exhibit similar UV absorption, with a pronounced absorption edge around 350 nm. $Bi_2O_2CO_3$ exhibits strong absorption at wavelengths below 350 nm, with a sharp edge at approximately 340 nm, typical of bismuth oxide compounds, which absorb primarily in the UV region due to their electronic structure [61]. $MoSi_2N_4$ shows the highest absorption, spanning 300–500 nm, with a sharp rise starting at 350 nm, indicative of its wide bandgap and broad UV–visible absorption [62]. These differences in absorption properties are essential for photocatalytic applications, with $MoSi_2N_4$ having the widest light absorption and MSN0.4-BOC performing well in the visible spectrum due to the functionalization.

Based on Fig. 5b, the Tauc plots derived from the UV–Vis absorption spectra were used to estimate the optical band gaps (E_g) of the samples using the $(\alpha h\nu)^2$ vs. $h\nu$ relationship. The calculated band gap values are 1.86 eV for $MoSi_2N_4$, 2.29 eV for MSN0.4–BOC, 2.73 eV for MSN0.2–BOC, and 3.12 eV for $Bi_2O_2CO_3$. Among them, $MoSi_2N_4$ exhibits the smallest band gap, indicating superior visible-light absorption capability and higher potential for photocatalytic activity [63]. In contrast, $Bi_2O_2CO_3$ displays the widest band gap, consistent with its primary UV-light absorption characteristics. Overall, the trend $MoSi_2N_4$ < MSN0.4–BOC < MSN0.2–BOC < $Bi_2O_2CO_3$ demonstrates the tunability of optical properties through structural and compositional modifications.

The photoluminescence (PL) spectra in Fig. 5c provide valuable insight into the recombination behavior of photoinduced charge carriers in the as-prepared samples. All samples exhibit a main emission band in the range of 380–450 nm, which originates from the radiative recombination of photogenerated electron–hole pairs. Among them, $MoSi_2N_4$ displays the strongest PL intensity, indicating a relatively high recombination rate of charge carriers. $Bi_2O_2CO_3$ shows a slightly weaker and broader emission centered around 425 nm, which can be attributed to defect-related Bi—O states. In contrast, the MSN0.4–BOC composite exhibits the lowest PL intensity, confirming that the interfacial interaction between $MoSi_2N_4$ and $Bi_2O_2CO_3$ effectively suppresses radiative recombination and promotes efficient charge separation. This reduced PL emission suggests improved carrier lifetime and enhanced photocatalytic activity for the composite system [64,65].

The time-resolved photoluminescence (TRPL) decay curves in Fig. 5d illustrate the carrier recombination dynamics of the samples. The MSN0.4–BOC composite exhibits the longest average lifetime of 4.32 ns, indicating effective charge separation and slower recombination of photogenerated carriers, both of which are beneficial for photocatalytic activity. In comparison, $Bi_2O_2CO_3$ shows a shorter lifetime of 3.98 ns, suggesting relatively faster carrier recombination that may limit its photocatalytic performance. $MoSi_2N_4$ exhibits an intermediate lifetime of 3.87 ns, indicating a moderate carrier-separation efficiency. The prolonged lifetime in MSN0.4–BOC can be attributed to the synergistic effect of the MSN, which facilitates charge transport and reduces recombination losses [66]. Overall, the TRPL results confirm that MSN0.4–BOC exhibits superior photoinduced charge-carrier dynamics compared to $Bi_2O_2CO_3$ and $MoSi_2N_4$, making it the most promising material for efficient photocatalytic applications.

The photocurrent response in Fig. 5e under periodic illumination shows the charge-transfer efficiency of the materials. The MSN0.4-BOC composite exhibits the highest photocurrent response, with a distinct, periodic increase in current upon light exposure, indicating efficient charge separation and transport. $MoSi_2N_4$ shows a moderate photocurrent response, consistent with its lower bandgap and broader light-absorption range. $Bi_2O_2CO_3$, however, shows a much weaker photocurrent, reflecting its poor charge transport properties, which is typical of Bi_2O_3-based materials. The photocurrent response of MSN0.4-BOC is higher, indicating its suitability for applications that require efficient electron transport and charge separation, such as in photocatalysis.

The EIS Nyquist plots in Fig. 5f provide insights into the electrochemical behavior and charge transfer resistance of the materials. The MSN0.4-BOC composite exhibits a low charge transfer resistance, with a semicircular arc at higher frequencies, indicating fast electron transport and efficient charge transfer at the interface. The $Bi_2O_2CO_3$ and $MoSi_2N_4$ samples exhibit larger arcs, indicating higher charge-transfer resistance and slower electron transport. The MSN0.4-BOC composite, with its smaller semicircle and lower impedance, indicates better electrochemical performance, making it more suitable for energy storage and catalytic applications where fast electron exchange is critical. The differences in the Nyquist plots reflect varying degrees of charge-transfer efficiency and resistance in each material, which are crucial factors in determining their performance in photocatalysis, energy storage, and other electrochemical applications.

3.5. Evaluation of photocatalytic performance

The data presented in Fig. 6 provides a comprehensive analysis of the photocatalytic properties of MSN0.2-BOC, MSN0.4-BOC, $MoSi_2N_4$, and $Bi_2O_2CO_3$ under various experimental conditions. All H_2O_2 production and DOX degradation experiments were performed in triplicate ($n = 3$) under identical conditions, and the reported results represent the mean of three independent runs. Fig. 6a shows the degradation of DOX (doxycycline) under both dark and light conditions, demonstrating that all materials exhibit significantly greater degradation under light exposure, a characteristic of photocatalytic processes. Among the materials tested, MSN0.4-BOC exhibits the highest degradation rate, achieving approximately 97% DOX degradation in 80 min under light, indicating its superior photocatalytic performance. In comparison, $MoSi_2N_4$ and $Bi_2O_2CO_3$ show slower degradation, reaching only 21% and 24%, respectively. These results suggest that MSN0.4-BOC is the most effective material for photocatalytic applications, which enhance light absorption and charge-carrier separation. The slow degradation observed in $MoSi_2N_4$ and $Bi_2O_2CO_3$ may be due to their slower charge transport and higher charge recombination rates, as evidenced by their lower H_2O_2 generation and photocurrent response [67].

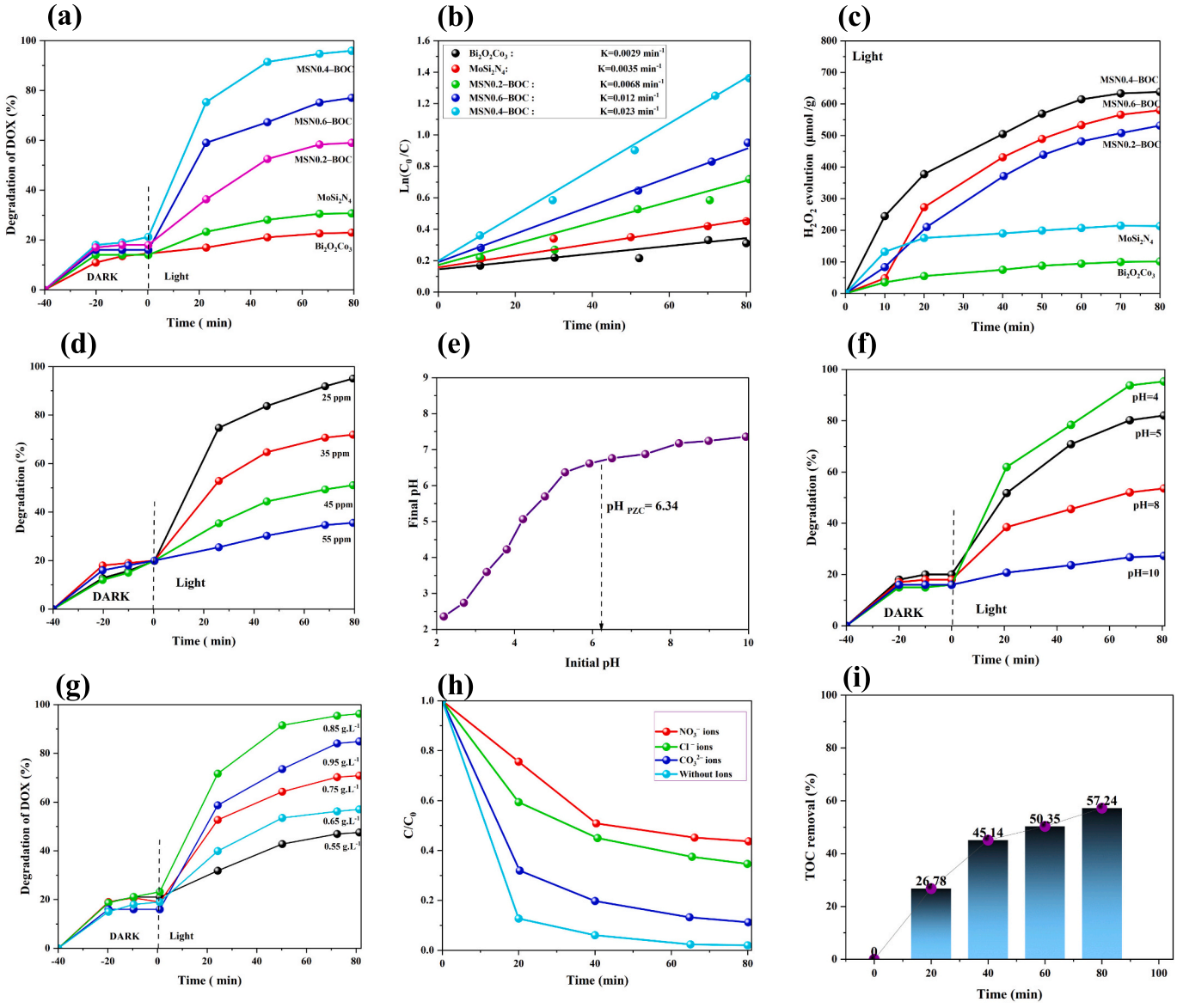

Fig. 6. (a) Degradation of DOX under dark and light conditions for different composites. (b) First-order kinetic plots for the degradation of DOX. (c) H_2O_2 generation under light irradiation. (d) Degradation of DOX at different initial concentrations. (e) pH calculation at the point of zero charge (pH pzc). (f) Degradation of DOX at different initial pH values. (g) Effect of catalyst dosage on DOX degradation. (h) Effect of ions (NO^{3-}, Cl^{-}, CO^{3-}) on DOX degradation. (i) Total organic carbon (TOC) removal efficiency over time.

The first-order kinetic plots in Fig. 6b confirm the enhanced photocatalytic performance of the MSN–BOC composites. The degradation of DOX follows a pseudo-first-order kinetic model, with rate constants (k) of 0.0029 min^{-1} for $Bi_2O_2CO_3$, 0.0035 min^{-1} for $MoSi_2N_4$, 0.0068 min^{-1} for MSN0.2–BOC, 0.012 min^{-1} for MSN0.6–BOC, and 0.023 min^{-1} for MSN0.4–BOC. Among these, MSN0.4–BOC exhibits the highest rate constant, indicating the fastest degradation rate and superior photocatalytic efficiency. In contrast, $Bi_2O_2CO_3$ shows the lowest reaction rate due to its wider bandgap and limited visible-light absorption.

Fig. 6c illustrates the H_2O_2 evolution performance of the photocatalysts under light irradiation. The H_2O_2 concentration was quantified using a titanium sulfate spectrophotometric method, and the measurements were calibrated using a pre-established standard calibration curve (Fig. S3a). Among all samples, MSN0.4–BOC shows the highest H_2O_2 generation (610 μmol g^{-1}), followed by MSN0.6–BOC (570 μmol g^{-1}) and MSN0.2–BOC (540 μmol g^{-1}). In contrast, $MoSi_2N_4$ (250 μmol g^{-1}) and $Bi_2O_2CO_3$ (180 μmol g^{-1}) exhibit much lower H_2O_2 yields due to faster charge recombination and weaker redox ability. The increased H_2O_2 production in MSN–BOC composites suggest more efficient charge separation and electron transfer under illumination. This enhanced ROS generation directly correlates with their superior photocatalytic degradation activity [68].

Fig. 6d shows the degradation of DOX at different initial concentrations, with MSN0.4-BOC exhibiting the most significant degradation at lower concentrations (25 ppm), with 97% degradation under light in 80 min. However, as the DOX concentration increases to 55 ppm, the degradation efficiency drops to around 32%. This decrease in efficiency with increasing concentration is typical of photocatalytic processes, where higher pollutant concentrations can saturate active sites on the catalyst surface, thereby reducing the material's effectiveness [69].

The pH_{pzc} (point of zero charge) for MSN0.4-BOC was determined to be 6.34, as shown in Fig. 6e. This value indicates the pH at which the material's surface charge is neutral, meaning it has an equal number of positive and negative charges [70]. At this pH_{pzc}, the material will have minimal interaction with pollutants, as the surface charge neither attracts nor repels ions. When the pH is below 6.34, the surface of MSN0.4-BOC becomes positively charged. This increases the material's ability to interact with negatively charged pollutants such as DOX [71]. The positive surface charge enhances the adsorption of negatively charged DOX molecules, thereby increasing the degradation rate [72]. As a result, MSN0.4-BOC performs most efficiently at pH 4, with nearly 95% DOX degradation after 80 min under light exposure. However, when the pH exceeds 6.34, the surface charge of MSN0.4-BOC becomes negative. This change in surface charge reduces the interaction between the material and negatively charged pollutants, thereby decreasing photocatalytic efficiency. At higher pH values (pH 8–10), the surface's negative charge repels the negatively charged DOX, resulting in a drop in degradation efficiency to about 50% (Fig. 6f). The material's effectiveness is thus reduced because the interaction with DOX becomes weaker.

Fig. 6g illustrates the influence of catalyst dosage on the photocatalytic degradation of DOX under visible-light irradiation. As the catalyst dosage increases from 0.55 to 0.85 g L^{-1}, the degradation efficiency steadily improves for all samples. The enhanced performance at higher catalyst loadings can be attributed to the greater number of available active sites and the increased light absorption, which generate more photoinduced charge carriers and ROS participating in the degradation process. For the MSN0.4–BOC composite, the degradation efficiency rises from about 50% at 0.55 g L^{-1} to nearly 96% at 0.85 g L^{-1}, outperforming the other catalysts across the entire range. This superior behavior indicates that MSN0.4–BOC possesses an efficient charge separation, and strong ROS generation capability, enabling rapid and complete DOX removal at higher catalyst dosages.

Fig. 6h illustrates the influence of different anions (NO_3^-, Cl^-, and CO_3^{2-}) on the photocatalytic degradation of DOX. In the absence of ions, the degradation efficiency reaches nearly 98% after 80 min, confirming the strong intrinsic activity of the photocatalyst. The presence of CO_3^{2-} ions slightly reduce degradation to about 85%, while Cl^- ions further reduce it to about 70%, indicating moderate inhibition. However, the addition of NO_3^- ions result in a pronounced decrease in activity, with only ≈50% degradation observed after 80 min. The strong inhibitory effect of NO_3^- is attributed to its electron-scavenging nature, which competes with O2 for photogenerated electrons, thereby reducing reactive oxygen species (ROS) formation. In contrast, CO_3^{2-} shows a minor promoting effect at initial stages, likely due to its buffering and charge-transfer assistance. Overall, the degradation trend follows Without ions > CO_3^{2-} > Cl^- > NO_3^-, highlighting the sensitivity of the photocatalytic system to ionic species in solution. Finally, Fig. 6i shows the TOC removal efficiency, with MSN0.4-BOC achieving 57.24% TOC removal after 80 min, which is significantly higher than that of both $Bi_2O_2CO_3$ and $MoSi_2N_4$. This indicates that MSN0.4-BOC not only degrades DOX effectively but also mineralizes the organic matter, breaking it down into simpler, non-toxic compounds. This high TOC removal efficiency is crucial for evaluating the overall efficiency of photocatalytic systems in treating organic pollutants.

3.6. Mechanistic elucidation of the Z–scheme charge transfer pathway

In Fig. 7, various analyses are performed to evaluate the photocatalytic properties of the materials MSN0.4-BOC, $Bi_2O_2CO_3$, $MoSi_2N_4$, and others under different experimental conditions. These include the effects of radical scavengers, electron-hole dynamics, and energy band structure, which provide critical insights into the degradation of DOX and the production of H_2O_2. Fig. 7a demonstrates DOX degradation under light exposure with different scavengers, showing how specific scavengers influence the photocatalytic process. The highest degradation rate is observed in the absence of scavengers, with approximately 97% degradation after 80 min. When BQ (benzoquinone), a scavenger for $\bullet O2^-$, is added, the degradation rate drops drastically to 13%, confirming that $\bullet O2^-$ plays a dominant role in the photocatalytic degradation of DOX. Similarly, the addition of EDTA-2Na, which scavenges h^+, reduces the degradation efficiency to 48%, while IPA, which scavenges •OH, results in a moderate reduction to 54%. These findings highlight the significant contribution of $\bullet O2^-$ and •OH radicals in the photocatalytic degradation process, with $\bullet O2^-$ being the most critical reactive species [73].

The ESR analyses shown in Fig. 7b and Fig. S3b provide compelling evidence for the light-induced formation of ROS in the MSN0.4–BOC photocatalytic system. In Fig. 7b, the characteristic quartet ESR signal of the DMPO–•OH adduct appears only under visible-light irradiation, with a markedly stronger intensity compared to the dark condition. This confirms that •OH are predominantly generated through light-activated oxidation pathways, consistent with the high valence-band potential of $Bi_2O_2CO_3$ in the *Z*-scheme heterojunction. The minimal ESR response in the dark further demonstrates that •OH formation is photo-driven and closely associated with the photocatalytic process. Complementarily, Fig. S3b displays the ESR spectra of DMPO–$\bullet O_2^-$, revealing the typical multi-line hyperfine splitting pattern associated with superoxide radical trapping. Under visible light, the ESR intensity increases significantly with irradiation time (5 to 10 min), indicating continuous generation of $\bullet O_2^-$ via the two-electron oxygen reduction reaction on $MoSi_2N_4$. The absence of a noticeable signal in the dark confirms that superoxide formation is strictly light-dependent.

Fig. S3c compares the photocatalytic degradation efficiency of DOX in distilled water and river water to evaluate the robustness of the MSN0.4–BOC catalyst under realistic environmental conditions. In distilled water, rapid degradation occurs after light irradiation, reaching nearly complete removal within 80 min. Although degradation in river water is slightly slower due to the presence of natural ions and organic impurities that compete for reactive species, the catalyst still maintains high activity, achieving more than 60% removal. These results confirm that MSN0.4–BOC exhibits strong tolerance to real-water matrices,

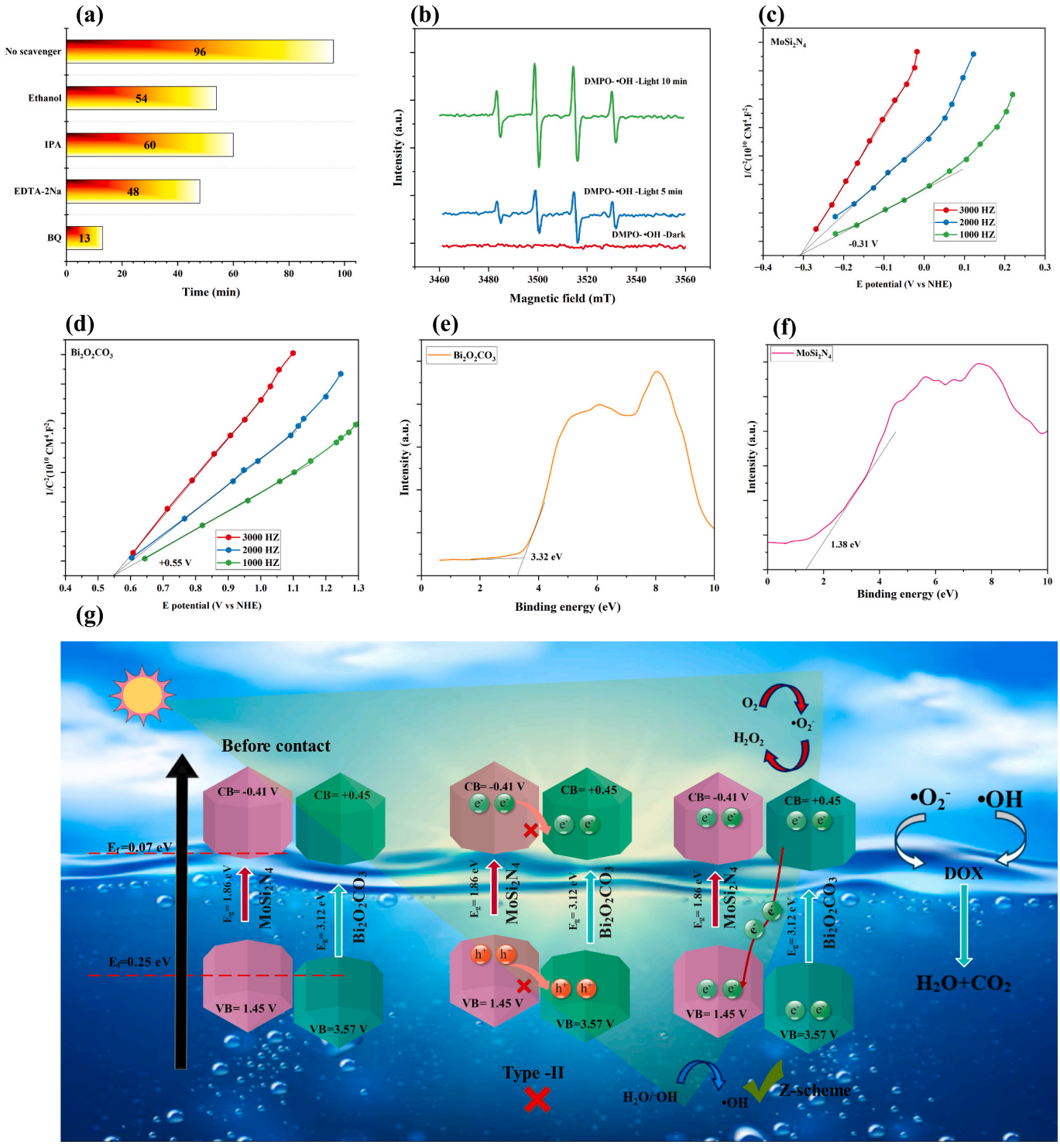

Fig. 7. (a) DOX degradation with different scavengers. (b) ESR spectra of DMPO-OH for $MoSi_2N_4$ under light and dark conditions. (c) Mott-Schottky plots for $MoSi_2N_4$. (d) Mott-Schottky plots for $Bi_2O_2CO_3$. (e) XPS valence band spectra of $Bi_2O_2CO_3$. (f) XPS valence band spectra of $MoSi_2N_4$. (g) Schematic of the Z-scheme mechanism for DOX degradation and H_2O_2 production.

demonstrating its practical applicability for environmental water treatment.

The Mott–Schottky plots in Fig. 7c and Fig. 7d reveal the flat-band potential (Vfb) and conduction band (CB) positions of the two materials. $MoSi_2N_4$ exhibits a Vfb of −0.31 V vs. NHE, corresponding to a CB position of approximately −0.41 V, indicating a moderate electron affinity and good electron-donating capability. In contrast, $Bi_2O_2CO_3$ shows a more positive Vfb of +0.55 V vs. NHE, resulting in a CB at +0.45 V, which suggests a stronger electron-accepting tendency compared to $MoSi_2N_4$. This potential difference between their CB levels facilitates efficient interfacial electron transfer in the *Z*-scheme heterojunction, enabling photogenerated electrons in $Bi_2O_2CO_3$'s CB to migrate to $MoSi_2N_4$, driving H_2O_2 production and pollutant degradation [74,75]. Further insights into the electronic structure are obtained from the XPS valence band (VB) spectra in Fig. 7e and Fig. 7f. The VB maximum of $Bi_2O_2CO_3$ is located at 3.32 eV, whereas $MoSi_2N_4$ has a

lower VB at 1.38 eV, confirming that $Bi_2O_2CO_3$ possesses a stronger oxidation potential suitable for degrading organic pollutants like DOX under visible light. Conversely, $MoSi_2N_4$'s lower VB makes it an efficient electron donor for H_2O_2 formation. The complementary band structures of $MoSi_2N_4$ and $Bi_2O_2CO_3$ enable effective electron–hole separation and directional charge transfer within the Z-scheme system. The Fermi levels (Ef), determined from the difference between the XPS VB positions and the calculated band edges, are 0.07 eV for $MoSi_2N_4$ and 0.25 eV for $Bi_2O_2CO_3$, indicating that $Bi_2O_2CO_3$ has a higher Ef and thus a greater tendency to accept electrons. This Fermi level offset promotes spontaneous electron transfer from $Bi_2O_2CO_3$ to $MoSi_2N_4$, driving redox reactions for both H_2O_2 evolution and pollutant oxidation [33,76]. Overall, the well-aligned CB, VB, and Ef levels confirm that the Z-scheme heterostructure effectively suppresses charge recombination, enhances visible-light utilization, and significantly improves photocatalytic efficiency for energy and environmental applications.

3.7. Identification of degradation intermediates and toxicity assessment

LC–MS analysis (Fig. S4) was conducted to identify the intermediate products formed during the photocatalytic degradation of DOX and to elucidate the corresponding oxidative pathways. As shown in Fig. 8a, the degradation process proceeds through two primary oxidative routes, Path I (P1 → P2 → P3) and Path II (P4 → P5 → P6 → P7 → P8), both ultimately leading to complete mineralization to CO2 and H_2O. Under visible-light irradiation, photogenerated holes and reactive oxygen species (mainly •OH and $•O_2^-$) first attack the amino-sugar and side chains of DOX, causing N-dealkylation, deamination, and cleavage of the glycosidic linkage. In Path I, removal of the side-chain and partial oxidation of the tetracyclic chromophore produces P1 (m/z = 355.82), in which the anthracycline core is retained. However, the sugar moiety is largely eliminated, and some hydroxyl groups are oxidized to carbonyl groups [77]. Further oxidative ring-opening and decarboxylation of this aromatic framework yields P2 (m/z = 231.47), a smaller polyoxygenated aromatic fragment [78]. Continued attack by •OH radicals causes additional demethylation and C—C bond cleavage, generating P3 (m/z = 110.01), a simple alkyl-substituted cyclic fragment that is then fully oxidized to CO2 and H_2O. In Path II, DOX undergoes initial hydroxylation and oxidative deamination to form P4 (m/z = 387.47), where the quinone-like structure becomes more oxygen-rich. Successive removal of hydroxyl and side-chain groups, accompanied by oxidation of secondary alcohols to carbonyls, leads to P5 (m/z = 339.97). Further oxidative ring contraction and cleavage of the fused aromatic system give rise to P6 (m/z = 215.74) and P7 (m/z = 149.01), which correspond to smaller bicyclic and benzylic intermediates [79]. Ultimately, deep oxidation of these aromatic fragments and scission of the remaining C—C bonds generate P8 (m/z = 72.47), a low-molecular-weight aliphatic species. P8 is then mineralized to CO_2 and H_2O.

In Fig. 8b, the acute toxicity of DOX and its degradation products toward Daphnia and Fathead minnow was analyzed to evaluate the environmental safety of the photocatalytic degradation process. The parent compound DOX exhibits very high toxicity, with LC_{50} values below 1 mg/L for both organisms, leading to severe mortality even at low concentrations. After photocatalytic degradation, the toxicity of all intermediates decreases significantly. For Daphnia, the LC_{50} values increase to approximately P1: 25 mg/L, P2: 110 mg/L, P3: 650 mg/L, P4: 1200 mg/L, P5: 850 mg/L, P6: 900 mg/L, P7: 1500 mg/L, and P8: 2000 mg/L, indicating that most products are classified as non-toxic or less harmful. A similar trend is observed for Fathead minnow, where DOX remains highly toxic (LC_{50} < 1 mg/L), while the intermediates show drastically lower toxicity: P1: 1.5 mg/L, P2: 5 mg/L, P3: 750 mg/L, P4: 1250 mg/L, P5: 400 mg/L, P6: 500 mg/L, P7: 1600 mg/L, and P8: 1900 mg/L. These results confirm that the photocatalytic degradation of DOX effectively reduces its ecotoxicity, transforming it into benign or non-

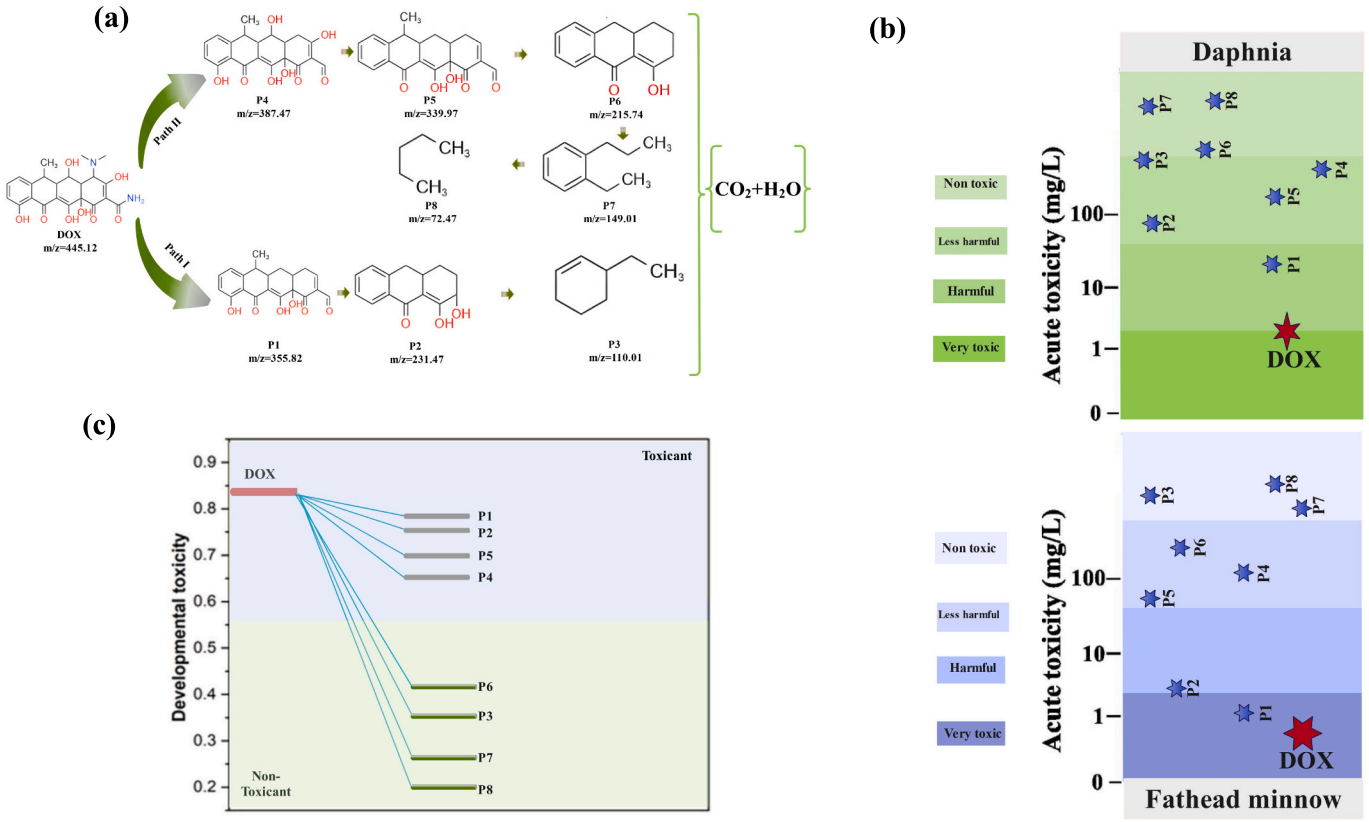

Fig. 8. (a) Proposed degradation pathway of DOX under photocatalytic conditions. (b) Acute toxicity of DOX and its degradation products on Daphnia and Fathead minnow. (c) Developmental toxicity and acute toxicity (LC50) analysis of DOX and degradation products.

toxic compounds. Overall, the data demonstrate that the degradation pathway leads to environmental detoxification, making the treated water considerably safer for aquatic organisms.

Fig. 8c illustrates the developmental toxicity of DOX and its photocatalytic degradation intermediates. The developmental toxicity score is a normalized index, where lower values indicate lower predicted toxicity and values closer to 1 indicate higher developmental toxicity. The parent compound DOX exhibits a high developmental toxicity score of about 0.85, classifying it as a strong toxicant capable of causing severe developmental abnormalities in aquatic organisms. After photocatalytic degradation, the toxicity of the intermediates decreases significantly. The early-stage products P1, P2, P4, and P5 exhibit moderate developmental toxicity values of 0.6–0.7, suggesting partial toxicity but far less harmful than DOX. In contrast, the later-stage degradation products P3, P6, P7, and P8 show much lower developmental toxicity scores (0.2–0.4), indicating that they are essentially non-toxic. Among these, P8 exhibits the lowest toxicity, confirming almost complete detoxification. The clear downward trend in developmental toxicity along the degradation pathway confirms that the photocatalytic process not only decomposes DOX structurally but also reduces its potential biological and ecological risks. Overall, the transformation of DOX into low-toxicity or non-toxic species underscores the environmental safety and effectiveness of photocatalytic treatment for pharmaceutical contaminants.

3.8. *Stability and reusability of the heterojunction catalyst*

Fig. 9 illustrates the stability and efficiency of a photocatalytic system in degrading DOX over multiple cycles, as well as the structural integrity of the catalyst after prolonged use. Fig. 9a presents the degradation efficiency of DOX across five cycling runs. Initially, the system achieves 97.25% degradation in the first cycle, demonstrating its high efficiency. However, over successive cycles, the degradation efficiency decreases slightly, dropping to 88.74% by the fifth cycle. This decline indicates a loss of catalytic activity after multiple cycles. However, it shows that the photocatalyst maintains relatively high performance, with only a 9.51% reduction in degradation efficiency over the five cycles. The results suggest that the catalyst retains good activity and efficiency for DOX degradation, even after several uses, making it a potentially viable option for repeated applications in wastewater treatment or for removing pharmaceutical pollution.

In Fig. 9b, the XRD patterns before and after the fifth cycle are compared to assess the structural stability of the photocatalyst. X-ray diffraction (XRD) analysis shows that the catalyst's diffraction peaks remain largely unchanged after five cycles of photocatalytic degradation. This suggests that the catalyst retains its crystallinity and structural integrity throughout the degradation process. The minimal shift in peak intensity or position indicates that the material does not undergo significant phase transformation or structural damage during cycling, which is essential for ensuring its long-term viability in practical applications. This stability is critical for industrial-scale applications, as it ensures the catalyst can be reused without significant structural degradation, maintaining high photocatalytic activity for sustained pollutant removal.

Table S3 provides a comparative overview of representative visible-light photocatalysts reported for H_2O_2 generation and pollutant removal. The comparison highlights differences in catalyst design, charge-transfer mechanisms, and performance metrics reported in the literature. Although direct numerical comparison is influenced by variations in reaction conditions and reporting units, the table demonstrates that the present MSN0.4-BOC system achieves competitive H_2O_2 production while simultaneously delivering efficient antibiotic removal and mineralization. This combined functionality and mechanistic validation distinguish the present work from many previously reported systems.

4. Conclusions and prospects

In summary, a novel *Z*-scheme $MoSi_2N_4$–$Bi_2O_2CO_3$ heterojunction photocatalyst was successfully fabricated through a hydrothermal–ultrasonic self-assembly approach, offering an efficient platform for simultaneous H_2O_2 production and DOX degradation under visible-light irradiation. Comprehensive structural and physicochemical characterizations, including XRD, XPS, Raman, FTIR, and TEM analyses, confirmed the intimate interfacial contact between $MoSi_2N_4$ nanosheets and $Bi_2O_2CO_3$ microplates. The well-defined heterointerface facilitated efficient charge migration across the junction, effectively suppressing electron–hole recombination and maintaining the strong redox potentials of both semiconductors. The optimized MSN0.4–BOC composite exhibited superior photocatalytic performance, achieving an H_2O_2 yield of 610 μmol g^{-1} h^{-1} and over 97% degradation efficiency of DOX, along with 57% TOC removal. Electrochemical and photophysical investigations, including EIS, photocurrent responses, and Mott–Schottky analyses, revealed enhanced charge separation and lower interfacial resistance due to the formation of a direct Z-scheme charge-transfer pathway. ESR and radical trapping experiments confirmed that •O2⁻

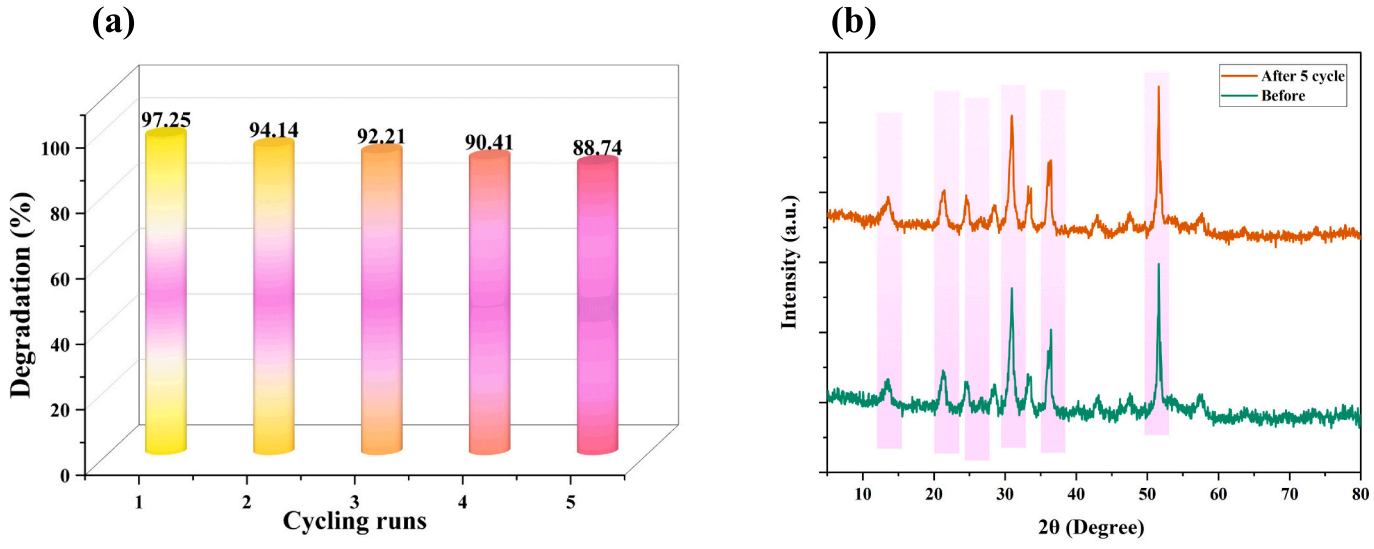

Fig. 9. (a) Degradation efficiency of DOX over five cycling runs. (b) XRD patterns before and after 5 cycling runs, showing the stability of the catalyst.

and •OH radicals played dominant roles in the oxidation and reduction processes. At the same time, LC–MS analysis identified the key intermediates and degradation pathways of DOX. Moreover, ecotoxicity assessments using Daphnia and Fathead minnow demonstrated that the photocatalytic treatment significantly reduced the acute and developmental toxicity of DOX and its byproducts. The photocatalyst retained its structural integrity and activity after five successive cycles, highlighting its excellent reusability and chemical stability. Future research should focus on scaling up the synthesis for large-scale wastewater treatment and continuous-flow systems. In-depth in situ spectroscopic and theoretical studies could further elucidate charge-transfer dynamics and the evolution of reactive species during photocatalysis. Additionally, coupling this *Z*-scheme system with other 2D materials or co-catalysts may further improve visible-light utilization and selectivity toward H_2O_2 production. The integration of such multifunctional heterostructures offers a promising pathway toward sustainable environmental remediation and solar-driven green chemical production.

CRediT authorship contribution statement

Rahila Batul: Writing – review & editing, Writing – original draft, Methodology, Funding acquisition, Data curation, Conceptualization. **Ali Alkhafaji:** Writing – review & editing, Writing – original draft, Data curation, Conceptualization. **Dheyaa J. Jasim:** Writing – review & editing, Writing – original draft, Resources, Methodology, Data curation, Conceptualization. **Pradeep Kumar Singh:** Writing – review & editing, Writing – original draft, Methodology, Investigation, Data curation, Conceptualization. **Y.M. Fahmy:** Writing – review & editing, Writing – original draft, Methodology, Funding acquisition, Formal analysis, Data curation, Conceptualization. **Mirsobit Odilov:** Writing – review & editing, Supervision, Software, Resources, Data curation. **Ibrahm Mahariq:** Writing – review & editing, Validation, Investigation, Data curation, Conceptualization. **Mukhtorjon Karimov:** Writing – review & editing, Visualization, Software, Resources, Formal analysis, Data curation, Conceptualization. **Nuraddin Abdullayev:** Writing – review & editing, Writing – original draft, Methodology, Formal analysis, Data curation, Conceptualization. **Reda A. Haggam:** Writing – review & editing, Writing – original draft, Validation, Resources, Methodology, Funding acquisition, Formal analysis, Data curation, Conceptualization.

Funding

This research was funded by the Deanship of Research and Graduate Studies at King Khalid University under grant number RGP.2/666/46.

Declaration of competing interest

The authors declare that they have no known competing financial interests or personal relationships that could have appeared to influence the work reported in this paper.

Acknowledgments

The authors extend their appreciation to the Deanship of Research and Graduate Studies at King Khalid University for funding this work through Large Group Project under grant number RGP.2/666/46.

Appendix A. Supplementary data

Supplementary data to this article can be found online at https://doi.org/10.1016/j.jwpe.2026.109580.

Data availability

No data was used for the research described in the article.

References

[1] H. Mikulčić, J. Baleta, Z. Zhang, J.J. Klemeš, Sustainable development of energy, water and environmental systems in the changing world, J. Clean. Prod. 390 (2023) 135945.
[2] M.S. Mohtaram, A. Abolghasemi, S. Sayahi, H. Rajabi, S. Mohtaram, M. Long, S. Sabbaghi, MOF-derived nanomaterials: transformative innovations for renewable energy and environmental sustainability, Coord. Chem. Rev. 546 (2026) 217083.
[3] M. Boujelbene, A. Basem, N.S. Alsaiari, S.A. Aldaghfag, M.A. Ismail, W. Rajhi, S. Ibragimova, A. Abilkasimov, Z. Atamuratova, Solar-driven dual-functional Z-scheme ZnIn2S4–Sb2O3 supported on activated carbon for simultaneous H2 generation and norfloxacin degradation: mechanism, analytical characterization, and toxicity assessment, Surf. Interfaces 75 (2025) 107785.
[4] S.D. Kayode-Afolayan, E.F. Ahuekwe, O.C. Nwinyi, Impacts of pharmaceutical effluents on aquatic ecosystems, Sci. Afr. 17 (2022) e01288.
[5] N.S. Sawaran Singh, A.B.M.. Ali, A.A.H.. Kadhum, M. Karimov, A. Abduvokhidov, O. Mukhitdinov, M. Shah, M.K. Al Mesfer, M. Danish, Plasmonic bi/IL-Bi2MoO6/T-gCN Z-scheme photocatalyst for enhanced visible-light degradation of organic contaminants, Surf. Interfaces 80 (2026) 108324.
[6] N.S. Sawaran Singh, A.B.M.. Ali, M. Shah, M.K. Al Mesfer, A. Abduvokhidov, A. Abilkasimov, D. Jumanazarov, E. Davletov, M.A. Diab, High-performance visible-light photocatalyst based on IL-modified Bi2MoO6 with MXene charge mediation and MIL-100(Fe) adsorptive oxidation for broad-spectrum aqueous remediation, Surf. Interfaces 76 (2025) 107929.
[7] V. Sonkar, V. Venu, B. Nishil, S. Thatikonda, Review on antibiotic pollution dynamics: insights to occurrence, environmental behaviour, ecotoxicity, and management strategies, Environ. Sci. Pollut. Res. 31 (2024) 51164–51196.
[8] M. Boujelbene, A.B.M. Ali, K. Alsaikhan, A. BaQais, M.B.B. Hamida, A. Amari, Y. Yusupov, A. Abduvokhidov, E. Khudoynazarov, Enhanced photocatalytic performance for organic pollutants degradation and H2O2 production using a novel rGO-bridged bi_2MoO_6-$CoTiO_3$ Z-scheme composites: analytical characterization, mechanism and toxicity assessment, Surf. Interfaces 72 (2025) 107201.
[9] K. Rasouli, J. Rasouli, M.S. Mohtaram, S. Sabbaghi, H. Kamyab, H. Moradi, S. Chelliapan, Biomass-derived activated carbon nanocomposites for cleaner production: a review on aspects of photocatalytic pollutant degradation, J. Clean. Prod. 419 (2023) 138181.
[10] Q. Yang, Y. Gao, J. Ke, P.L. Show, Y. Ge, Y. Liu, R. Guo, J. Chen, Antibiotics: An overview on the environmental occurrence, toxicity, degradation, and removal methods, Bioengineered 12 (2021) 7376–7416.
[11] Z.H. Jabbar, B.H. Graimed, A.A. Okab, S.H. Ammar, H. Taofeeq, M. Al-Yasiri, Synthesis of 3D Sb2O3-based heterojunction reinforced by SPR effect and photo-Fenton mechanism for upgraded oxidation of metronidazole in water environments, J. Environ. Manage. 362 (2024) 121347.
[12] Y. Yang, A.B.M. Ali, S.A. Aldaghfag, H. Lin, H. Elmonser, I. Mahariq, B. Saydullaev, M. Karimov, M. Seytnazarov, R.A. Haggam, Dual-functional Z-scheme MgIn2S4/WO3 heterojunction for visible-light CO2 reduction and antibiotic degradation: unraveling charge transfer and reaction mechanisms, Sep. Purif. Technol. (2026) 136908, https://doi.org/10.1016/j.seppur.2026.136908.
[13] J. Yang, X. Zeng, M. Tebyetekerwa, Z. Wang, C. Bie, X. Sun, I. Marriam, X. Zhang, Engineering 2D Photocatalysts for solar hydrogen peroxide production, Adv. Energy Mater. 14 (2024) 2400740.
[14] Y. Bu, R. Ma, Y. Wang, Y. Zhao, F. Li, G.-F. Han, J.-B. Baek, Metal-based oxygen reduction Electrocatalysts for efficient hydrogen peroxide production, Adv. Mater. 36 (2024) 2412670.
[15] B. Wang, X. Feng, Y. Liu, X. Wang, E. Liu, Y. Zhao, Z. Miao, Z. Li, Ultrafast electron transfer coupled with a proton relay in an anisotropic dual S-scheme heterojunction for overcoming kinetics mismatch in H2O2 photosynthesis, Adv. Sci. (2025) e22285.
[16] A.A. Ingle, S.Z. Ansari, D.Z. Shende, K.L. Wasewar, A.B. Pandit, Progress and prospective of heterogeneous catalysts for H2O2 production via anthraquinone process, Environ. Sci. Pollut. Res. 29 (2022) 86468–86484.
[17] Z. Jiang, C. Li, F. Qi, Z. Wang, Y. Liu, F. Li, H. Wang, Z. Bian, M. Zhu, J. Kumirska, E.M. Siedlecka, A review on photocatalytic hydrogen peroxide production from oxygen: material design, mechanisms, and applications, ACS Appl. Mater. Interfaces 17 (2025) 42–66.
[18] Z.H. Jabbar, B.H. Graimed, A.A. Okab, S.H. Ammar, M.A. Hussein, A. Majdi, Generation of robust chemical oxidants induced by solar-light radiation over binary Bi12O17Cl2/Ag2CrO4 photocatalyst with type I heterojunction: Enrofloxacin degradation activity, Sol. Energy 287 (2025) 113216.
[19] Y. Shen, R. Xu, P. Shan, S. Zhang, L. Sun, H. Xie, F. Guo, C. Li, W. Shi, Abundant edge active sites-modified high-crystalline g-C3N5 for hydrogen peroxide production from pure-water via a quasi-homogeneous photocatalytic process, Small 20 (2024) 2401566.
[20] S. Wang, Z. Xie, D. Zhu, S. Fu, Y. Wu, H. Yu, C. Lu, P. Zhou, M. Bonn, H.I. Wang, Q. Liao, H. Xu, X. Chen, C. Gu, Efficient photocatalytic production of hydrogen peroxide using dispersible and photoactive porous polymers, Nat. Commun. 14 (2023) 6891.
[21] Z.H. Jabbar, B.H. Graimed, S.H. Ammar, H. Taofeeq, M.M.B. Alsunbuli, S.M. Al-Jubouri, A.H. Abbar, M.J. M-Ridha, A.G. Taher, A critical review describes wastewater photocatalytic detoxification over Bi5O7I-based heterojunction photocatalysts: characterizations, mechanism insight, and DFT calculations, journal of environmental, Chem. Eng. 12 (2024) 112241.
[22] Y. Ding, S. Maitra, S. Halder, C. Wang, R. Zheng, T. Barakat, S. Roy, L.-H. Chen, B.-L. Su, Emerging semiconductors and metal-organic-compounds-related

photocatalysts for sustainable hydrogen peroxide production, Matter 5 (2022) 2119–2167.
[23] Y. Guo, X. Tong, N. Yang, Photocatalytic and electrocatalytic generation of hydrogen peroxide: principles, catalyst design and performance, Nano-Micro Lett. 15 (2023) 77.
[24] M.S. Mohtaram, S. Mohtaram, S. Sabbaghi, X. You, W. Wu, L. Jia, K. Muzammil, N. A. Alraee, S. Islam, Y. Aryanfar, Photocatalytic degradation of acetaminophen using a novel TiO2-orange peel-derived biochar composite: synthesize, characterization and optimization of key factors, J. Water Process Eng. 58 (2024) 104884.
[25] M.S. Mohtaram, S. Sabbaghi, J. Rasouli, K. Rasouli, Photocatalytic degradation of tetracycline using a novel WO3–ZnO/AC under visible light irradiation: optimization of effective factors by RSM-CCD, Environ. Pollut. 347 (2024) 123746.
[26] Z. Chen, J. Li, J. Zhang, H. Wang, Y. Zeng, F. Wang, P. Huang, X. Chen, L. Ge, R. A. Dahlgren, H. Gao, X. Huang, A highly efficient and recyclable living biocatalyst using Shewanella@polydopamine@NH2-doped carbon dot biohybrids and polypyrrole immobilized melamine foam for microbial-photoreduction of Cr(VI), J. Clean. Prod. 435 (2024) 140497.
[27] X. Li, H. Sun, Y. Xie, Y. Liang, X. Gong, P. Qin, L. Jiang, J. Guo, C. Liu, Z. Wu, Principles, synthesis and applications of dual Z-scheme photocatalysts, Coord. Chem. Rev. 467 (2022) 214596.
[28] J. Abdul Nasir, A. Munir, N. Ahmad, T.u. Haq, Z. Khan, Z. Rehman, Photocatalytic Z-scheme overall water splitting: recent advances in theory and experiments, Adv. Mater. 33 (2021) 2105195.
[29] P. Zhao, L. Zhang, X. Yu, Z. Wang, R. Han, Y. Jia, P. Zhao, Enhanced photocatalytic activity via dual Z-scheme charge separation in BiOBr/BiOCl/Bi2O2CO3 ternary heterojunction for organic contaminant removal, J. Alloys Compd. 1041 (2025) 183856.
[30] C. Wu, H. Zuo, H. Du, S. Zhang, L. Wang, Q. Yan, Construction of layered embedding dual Z-scheme Bi2O2CO3/g-C3N4/Bi2O3: tetracycline degradation pathway, toxicity analysis and mechanism insight, Sep. Purif. Technol. 282 (2022) 120096.
[31] Y. Wang, L. Ding, C. Liu, Y. Lu, Q. Wu, C. Wang, Q. Hu, 0D/2D/2D ZnFe2O4/Bi2O2CO3/BiOBr double Z-scheme heterojunctions for the removal of tetracycline antibiotics by permonosulfate activation: photocatalytic and non-photocatalytic mechanisms, radical and non-radical pathways, Sep. Purif. Technol. 283 (2022) 120164.
[32] P. Lai, J. Li, Z. Xu, B. Wang, G. Li, In-situ constructed Z-scheme Bi2O2CO3/g-C3N4 heterojunction: enhanced photocatalytic degradation of preservatives, Sep. Purif. Technol. 382 (2026) 135892.
[33] S. Wang, X. Jin, Facile construction of Z-scheme CAU-17/Bi2O2CO3 heterojunction for high-efficiency photocatalytic pollutant degradation, Appl. Surf. Sci. 711 (2025) 164063.
[34] A. Jalil, T. Zhao, A. Kanwal, I. Ahmed, Prediction of direct Z-scheme H and Ḣ-phase of MoSi2N4/MoSX (X = S, se) van der Waals heterostructures: a promising candidate for photocatalysis, Chem. Eng. J. 470 (2023) 144239.
[35] L. Xu, Y. Zhang, Z. Ma, T. Chen, C. Guo, C. Wu, H. Li, X. Huang, S. Tang, L.-L. Wang, Indirect Z-scheme hydrogen production photocatalyst based on two-dimensional GeC/MoSi2N4 van der Waals heterostructures, Int. J. Hydrogen Energy 48 (2023) 18301–18314.
[36] N. Zhao, J. Wang, Z. Cui, S-scheme MoSi2N4/AlN with a 2D heterojunction for photocatalytic water dissociation, Acta Mater. 285 (2025) 120655.
[37] J. Wang, Q. Chu, M. Xu, Y. Gong, Y. Feng, M. Meng, M. Gao, Construction of a BiOCl/Bi2O2CO3 S-scheme heterojunction Photocatalyst via sharing [Bi2O2]2+ slabs with enhanced photocatalytic H2O2 production performance, Langmuir 40 (2024) 15456–15467.
[38] C. Zhou, X.-l. Wang, H. Yu, M. Yang, X.-t. Dong, Y. Yang, Preparation and properties of 3D spherical Bi2S3/Bi2O2CO3 photocatalytic materials self-assembled by 2D nanosheets, Appl. Organomet. Chem. 38 (2024) e7727.
[39] Y. Chang, P. Bai, X. Zhao, X. Cui, Exploring hot carrier relaxation dynamics in MoSi2N4 monolayer for photocatalytic applications: insights into electron-phonon coupling mechanisms, Appl. Surf. Sci. 664 (2024) 160237.
[40] J. Mo, L. Li, X. Li, X. Yao, X. Xiang, X. Zu, First-principles study of a novel type-II As2C3/MoSi2N4 heterostructure with high carrier mobility in photocatalytic water splitting, Int. J. Hydrogen Energy 100 (2025) 982–993.
[41] S. Wang, C. Li, H. Yin, B. Gao, Z. Yu, Y. Zhou, J. Wang, H. Xu, J. Wu, Y. Sun, A novel ag/bi/Bi2O2CO3 photocatalyst effectively removes antibiotic-resistant bacteria and tetracycline from water under visible light irradiation, Environ. Res. 264 (2025) 120313.
[42] P. Xiao, C. Shen, Y. Li, S. Cui, S. Chen, J. Yang, A one-pot hydrothermal synthesis of bi/Bi2O2CO3/Bi2WO6 catalyst with enhanced photocatalytic activity to tetracycline, J. Taiwan Inst. Chem. Eng. 162 (2024) 105611.
[43] H. Zhao, Y. Dong, P. Sun, Y. Bai, C. Ru, X. Wu, Z. Li, X. Han, J. Wu, X. Pan, Effect of D/a ratio on photocatalytic hydrogen evolution performance of conjugated polymer Photocatalysts, ACS Appl. Energy Mater. 5 (2022) 4631–4640.
[44] A. Das, R.G. Nair, Effect of aspect ratio on photocatalytic performance of hexagonal ZnO nanorods, J. Alloys Compd. 817 (2020) 153277.
[45] Z. Chu, J. Li, H.Y. Sohn, C. Chen, X. Huang, Y. Lan, A. Murali, J. Zhang, CeO2-g-C3N4 S-scheme heterojunctions for enhanced photocatalytic performance: effects of surface C/N ratio on photocatalytic and adsorption properties, Compos. Part B Eng. 257 (2023) 110689.
[46] J. Yu, G. Wang, B. Cheng, M. Zhou, Effects of hydrothermal temperature and time on the photocatalytic activity and microstructures of bimodal mesoporous TiO2 powders, Appl. Catal. Environ. 69 (2007) 171–180.
[47] D. Wu, M. Long, W. Cai, C. Chen, Y. Wu, Low temperature hydrothermal synthesis of N-doped TiO2 photocatalyst with high visible-light activity, J. Alloys Compd. 502 (2010) 289–294.
[48] L. Mao, B. Lu, J. Shi, Y. Zhang, X. Kang, Y. Chen, H. Jin, L. Guo, Rapid high-temperature hydrothermal post treatment on graphitic carbon nitride for enhanced photocatalytic H2 evolution, Catal. Today 409 (2023) 94–102.
[49] S. Xia, C. Wei, Y. Zhai, B. Ding, J. Yu, J. Yan, Ultrasonic cavitation enhanced photocatalytic CO2 reduction by superior flexible black BaTiO3 nanofibers, Chem. Eng. J. 475 (2023) 146516.
[50] M.R. Ardani, A.L. Pang, U. Pal, R. Zheng, A. Arsad, A.A. Hamzah, M. Ahmadipour, Ultrasonic-assisted polyaniline-multiwall carbon nanotube photocatalyst for efficient photodegradation of organic pollutants, J. Water Process Eng. 46 (2022) 102557.
[51] K. Rasouli, A. Alamdari, S. Sabbaghi, Ultrasonic-assisted synthesis of α-Fe2O3@TiO2 photocatalyst: optimization of effective factors in the fabrication of photocatalyst and removal of non-biodegradable cefixime via response surface methodology-central composite design, Sep. Purif. Technol. 307 (2023) 122799.
[52] Y. Huang, X. Zhang, F. Zheng, S. Zou, M. Li, P. Huang, Y. Zeng, Controlled synthesis of β-Bi2O3/Bi2O2CO3 hollow microspheres with enhanced photocatalytic degradation of tetracycline under visible light, Mater. Today Commun. 33 (2022) 104304.
[53] Q. Wang, S. Li, G. Yuan, Z. Cheng, Z. Yang, H. Lv, Z. Peng, C. Han, W. Zou, F. Nemangwele, J. Liu, X. Ma, All-solid-state S-scheme heterojunction TiO2/cu/MoSi2N4 for efficient visible-light driven water splitting, Small Methods 9 (2025) 2402265.
[54] X. Zu, Y. Zhao, X. Li, R. Chen, W. Shao, Z. Wang, J. Hu, J. Zhu, Y. Pan, Y. Sun, Y. Xie, Ultrastable and efficient visible-light-driven CO2 reduction triggered by regenerative oxygen-vacancies in Bi2O2CO3 Nanosheets, Angew. Chem. Int. Ed. 60 (2021) 13840–13846.
[55] Z. Deng, Electric field enhancement effect on Raman spectra in two-dimensional MoSi2N4, TiSi2N4 and MoGe2As4 monolayers, Solid State Commun. 358 (2022) 114994.
[56] Y. Xiao, D. Liu, J. Yang, J. Feng, W. Gu, L. Qiao, W.F. Ip, H. Pan, Controllable reconstruction of β-Bi2O3/Bi2O2CO3 composite for highly efficient and durable electrochemical CO2 conversion, Nano Lett. 25 (2025) 6548–6555.
[57] S. Zhu, X. Wen, J. Zeng, C. Wang, X. Luo, A facile way for one-pot synthesis of porous rose-like β-Bi2O3/Bi2O2CO3 with enhanced photocatalytic activity for BPA photodegradation, J. Mater. Sci. 57 (2022) 19356–19370.
[58] R. Du, J. Zhang, X. Zhang, C. Feng, H. Jin, Y. Wang, Y. Zhou, R. Chong, In-situ growth into jungle-like Bi2O3/Bi2O2CO3 heterostructures with concentration-controllable oxygen vacancy and ratio-tunable phase composition, Mater. Sci. Semicond. Process. 150 (2022) 106893.
[59] D. Huang, F. Liang, R. Guo, D. Lu, J. Wang, H. Yu, H. Zhang, Exciton self-trapping effect in MoSi2N4 for modulating nonlinear optical process, Adv. Opt. Mater. 11 (2023) 2202622.
[60] C. Lai, F. Xu, M. Zhang, B. Li, S. Liu, H. Yi, L. Li, L. Qin, X. Liu, Y. Fu, N. An, H. Yang, X. Huo, X. Yang, H. Yan, Facile synthesis of CeO2/carbonate doped Bi2O2CO3 Z-scheme heterojunction for improved visible-light photocatalytic performance: Photodegradation of tetracycline and photocatalytic mechanism, J. Colloid Interface Sci. 588 (2021) 283–294.
[61] M.A. Wahba, S.M. Yakout, Y.K. Abdel-Monem, A.A.A. Hammood, Simple and easy control-synthesis of pure α-Bi2O3 and Bi2O2CO3: morphological, optical and solar photon-energy photocatalytic studies, Chem. Afr. 7 (2024) 195–207.
[62] W. Zhang, J. Guo, X. Lv, F. Zhang, Combined machine learning and high-throughput calculations predict Heyd–Scuseria–Ernzerhof band gap of 2D materials and potential MoSi2N4 Heterostructures, J. Phys. Chem. Lett. 15 (2024) 5413–5419.
[63] N. Plubphon, S. Thongtem, A. Phuruangrat, C. Randorn, S. Kaowphong, T. Thongtem, Microwave-assisted synthesis and enhanced photocatalytic performance of Bi2O2CO3 nanoplates, Inorg. Chem. Commun. 134 (2021) 109004.
[64] D. Wrana, T. Gensch, B.R. Jany, K. Cieślik, C. Rodenbücher, G. Cempura, A. Kruk, F. Krok, Photoluminescence imaging of defects in TiO2: the influence of grain boundaries and doping on charge carrier dynamics, Appl. Surf. Sci. 569 (2021) 150909.
[65] Z. Li, D. Liao, G. Tian, X. Fan, X. Chai, W. Chang, Y. Gao, B. Yuan, Z. Li, F. Wei, C. Zhang, Determination of Mn valence states in Nanocatalysts during sustainable syngas conversion, J. Am. Chem. Soc. 147 (2025) 32548–32559.
[66] Z. Qu, Y. Zhao, F. Ma, L. Mei, X.-K. Chen, H. Zhou, X. Chu, Y. Yang, Q. Jiang, X. Zhang, J. You, Enhanced charge carrier transport and defects mitigation of passivation layer for efficient perovskite solar cells, Nat. Commun. 15 (2024) 8620.
[67] Y. Fang, L. Hong, Y. Dai, Q. Xiang, N. Zhang, J. Li, Reconstruction of the surface Bi3+ oxide layer on Bi2O2CO3: facilitating electron transfer for enhanced photocatalytic degradation performance of antibiotics in water, Ceram. Int. 50 (2024) 52788–52796.
[68] H. Liu, M. Yan, Z. Wang, G. Xie, X. Pu, Y. Fu, X. Peng, H. Wang, J. Wang, Constructing boosted charge separation for efficient H2O2 production and pollutant degradation by highly defective ZnIn2S4/carbon doped boron nitride, J. Environ. Chem. Eng. 12 (2024) 114251.
[69] A. Fatima, J. Akhtar, K.H. Thebo, M. Kazi, Enhanced photocatalytic degradation of doxycycline over Titania under visible light, Arab. J. Sci. Eng. 50 (2025) 6639–6653.
[70] S. Salesi, A. Nezamzadeh-Ejhieh, An experimental design study of photocatalytic activity of the Z-scheme silver iodide/tungstate binary nano photocatalyst, Environ. Sci. Pollut. Res. 30 (2023) 105440–105456.
[71] J. Rasouli, M. Binazadeh, S. Sabbaghi, Synthesis of a novel biomass waste-based photocatalyst for degradation of high concentration organic pollutants under

visible light: optimization of synthesis condition and operational parameters via RSM-CCD, Surf. Interfaces 49 (2024) 104400.
[72] Y. Dong, X. Wang, H. Sun, X. Zhao, H. Zhang, L. Chen, D. Huang, Y. Yang, J. Zheng, L. Wang, Constructing a stable photocatalytic functional layer through cross-linking of chitosan and l-mannose for efficient removal of doxycycline hydrochloride in single-pass flow mode, J. Membr. Sci. 709 (2024) 123154.
[73] H. Fan, X. Ma, X. Li, L. Yang, Y. Bian, W. Li, Fabrication of novel g-C3N4@bi/Bi2O2CO3 Z-scheme heterojunction with meliorated light absorption and efficient charge separation for superior photocatalytic performance, Molecules (2022) 8336.
[74] H. Du, Y. Ma, X. Du, W. Zhang, X. Chen, 3D/2D CuBi2O4@Bi2O2CO3 Z-scheme heterojunction: the construction of adsorption-photocatalytic synergistic effect for tetracycline hydrochloride removal, J. Environ. Chem. Eng. 11 (2023) 110501.
[75] H.D. Abdul Kader, S.H. Ammar, W.A. Abdulnabi, M.A. Lafta, Z.H. Jabbar, Assembly of Br-doped graphitic-C3N4 decorated with AgVO3 nanoribbons as efficient Z-type photocatalyst heterojunctions for decontamination of bisphenol a (BPA), Inorg. Chem. Commun. 177 (2025) 114363.
[76] T. Guan, J. Wu, Z. Shi, B. Chen, W. Gao, N. Zhao, K. Xie, Y. Liu, P. He, K. Huang, Stable oxygen vacancies together with dynamic shuttling of I−/IO3− to promote the photocatalytic oxidation activity of BiOIO3/Bi2O2CO3 Z-scheme heterojunctions, Sep. Purif. Technol. 370 (2025) 133197.
[77] P.R. Sivaranjani, V. Subhiksha, M.K. Okla, B. Janani, M.A. Abdel-Maksoud, S.S. Al-Amri, I.A. Alaraidh, A.A. Alatar, S.S. Khan, Construction of p-n-p nano heterojunction through coupling La2O3, (BiO)2CO3 and Ag3PO4 for effective photocatalytic degradation of doxycycline: insights into mechanism, pathway and intermediate toxicity evaluation, Environ. Pollut. 345 (2024) 123521.
[78] W. Liu, Q. Kang, L. Wang, L. Wen, Z. Li, Facile synthesis of Z-scheme g-C3N4@MIL-100 (Fe) and the efficient photocatalytic degradation on doxycycline and disinfection by-products by coupling with persulfate: mechanism and pathway, Colloids Surf. A Physicochem. Eng. Asp. 635 (2022) 128057.
[79] S. Balasurya, M.K. Okla, H. AbdElgawad, A.A. Al-ghamdi, M.A. Abdel-Maksoud, S. S. Al-Amri, M.M.Y. Madany, S.S. Khan, Sunlight promoted self-Fenton photodegradation and pathway of doxycycline: interactive effects of nanomaterial on bean plant and its genotoxicity against Allium cepa, Chemosphere 313 (2023) 137286.